The Influence of Shear on Deep Convection Initiation. Part II: Simulations

JOHN M. PETERS,[a] HUGH MORRISON,[b] T. CONNOR NELSON,[c] JAMES N. MARQUIS,[d] JAKE P. MULHOLLAND,[a] AND CHRISTOPHER J. NOWOTARSKI[e]

[a] *Department of Meteorology, Naval Postgraduate School, Monterey, California*
[b] *National Center for Atmospheric Research, Boulder, Colorado*
[c] *Department of Atmospheric and Oceanic Sciences, University of Colorado Boulder, Boulder, Colorado*
[d] *Pacific Northwest National Laboratory, Richland, Washington*
[e] *Department of Atmospheric Science, Texas A&M University, College Station, Texas*

(Manuscript received 24 May 2021, in final form 26 January 2022)

ABSTRACT: This study evaluates a hypothesis for the role of vertical wind shear in deep convection initiation (DCI) that was introduced in Part I by examining behavior of a series of numerical simulations. The hypothesis states, "Initial moist updrafts that exceed a width and shear threshold will 'root' within a progressively deeper steering current with time, increase their low-level cloud-relative flow and inflow, widen, and subsequently reduce their susceptibility to entrainment-driven dilution, evolving toward a quasi-steady self-sustaining state." A theoretical model that embodied key elements of the hypothesis was developed in Part I, and the behavior of this model was explored within a multidimensional environmental parameter space. Remarkably similar behavior is evident in the simulations studied here to that of the theoretical model, both in terms of the temporal evolution of DCI and in the sensitivity of DCI to environmental parameters. Notably, both the simulations and theoretical model experience a bifurcation in outcomes, whereby nascent clouds that are narrower than a given initial radius R_0 threshold quickly decay and those above the R_0 threshold undergo DCI. An important assumption in the theoretical model, which states that the cloud-relative flow of the background environment V_{CR} determines cloud radius R, is scrutinized in the simulations. It is shown that storm-induced inflow is small relative to V_{CR} beyond a few kilometers from the updraft edge, and V_{CR} therefore plays a predominant role in transporting conditionally unstable air to the updraft. Thus, the critical role of V_{CR} in determining R is validated.

KEYWORDS: Convective clouds; Cumulus clouds; Severe storms; Storm environments; Supercells; Conservation of mass; Convective storms

1. Introduction

Recent modeling studies argue that vertical wind shear inhibits the growth rate of cumulus congestus clouds (Peters et al. 2019a; Nelson et al. 2021) via downward-oriented dynamic pressure accelerations that suppress cloud growth rates (referred to as the "shear suppression effect"). This process may negatively influence the probability of deep convection initiation (DCI). However, this purported negative relationship between vertical wind shear and DCI is somewhat at odds with other research findings (Peters et al. 2019b), which show that vertical wind shear organizes and widens updrafts, and subsequently reduces updrafts' susceptibility to entrainment-driven dilution. These seemingly contradictory notions underscore the lack of a comprehensive understanding of how vertical wind shear (hereafter "shear") influences DCI over a wide range of environmental scenarios. To reconcile these ideas in Peters et al. (2022, hereafter Part I), we introduced the following hypothesis: Shear can positively influence DCI via what we call the "progressive rooting hypothesis," whereby updrafts may root within a sufficiently strong steering current to increase their low-level cloud-relative inflow and widen with time. The progressive widening shields an updraft core from entrainment-driven dilution, allowing the updraft to deepen and further widen. This leads to a positive feedback cycle whereby the updraft eventually achieves a quasi-steady-state width and depth. In this "progressive rooting regime," the entrainment-reducing effects of shear dominate over the shear suppression effect, and shear helps to facilitate DCI. When this feedback cycle does not occur, shear generally inhibits updraft deepening through the shear suppression effect. In this "shear suppression regime," the negative influences of the shear suppression dominate over the entrainment reducing effects of shear, and shear generally slows or prevents DCI.

We elaborated on this hypothesis in Part I by developing a theoretical model for updraft evolution, that originated from simplifications of the basic equations that govern cloud-scale motions. We examined the model's behavior in a large parameter space of shear s, initial subcloud updraft radius R_0, free-tropospheric relative humidity (RH), and convective available potential energy (CAPE), with the assumption that any ambient convective inhibition (CIN) has been removed. The behavior of this theoretical model suggests that the degree to which shear "helps or hurts" DCI depends strongly on the initial combination of the aforementioned environmental parameters. For instance, when R_0, RH, and CAPE are all large, DCI benefits from shear via the mechanism described in the progressive rooting hypothesis because updrafts become wider and faster with larger s. However, for smaller R_0, RH, and CAPE, shear has a negative influence on DCI, inhibiting updraft growth in a manner consistent with the

Corresponding author: John M. Peters, jmpeters@nps.edu

DOI: 10.1175/JAS-D-21-0144.1

shear suppression effect. Furthermore, there is a shear threshold (which is dependent on R_0, CAPE, and RH) below which DCI is suppressed by shear, and above which DCI is facilitated by shear.

The overarching objectives of Part II of this study are to determine whether updrafts produced in cloud-resolving simulations behave consistently with the theoretical model, thereby validating our hypothesis. We address the following specific questions.

a. Do simulated updrafts behave like those in the theoretical model?

If our hypothesis and theoretical model are valid, the behavior of convection in both the simulations and the theoretical model should embody the shear suppression effect and progressive rooting hypothesis in a qualitatively similar way. This behavior includes correlations between cloud-relative flow (V_{CR}; see Table 1 for summary of symbol definitions), updraft radius R, and updraft depth H within a given simulation, and among separate simulations. Further, the simulations should exhibit a similar "tipping point" in R_0 to that of the theoretical model, whereby a sharp R_0 cutoff determines whether or not simulations produce quasi-steady sustained or dissipating convection. In the cases where simulations produce steady updrafts, R should evolve toward a common steady value for a range of different R_0. Finally, the rate of initial updraft growth should be slower in strongly sheared simulations, relative to weakly sheared simulations. We therefore examine the simulations for evidence of consistent behavior between the simulations and the theoretical model.

b. How valid is the assumption that cloud inflow is exclusively determined by environmental cloud-relative flow (V_{CR})?

To provide context for this question, we must precisely define what we mean by "inflow" (hereafter V_{IN}) and V_{CR}. The inflow at any point along the updraft periphery is defined as the velocity of air as it flows inward across the periphery, relative to the cloud motion. Cloud-relative flow, on the other hand, is the difference between the cloud's far-field environmental wind profile and the cloud motion. Perhaps the most important assumption in Part I is that inflow is determined by the V_{CR} of air that encounters the updraft periphery, implying a monotonic relationship between V_{CR} and inflow. Since inflow and updraft width are connected via mass continuity (Peters et al. 2019b), this assumed relationship between inflow and V_{CR} means that small V_{CR} equates to a narrow updraft and large V_{CR} equates to a wide updraft. Thus, if this relationship holds over a range of environments, V_{CR} can be used to predict updraft R. Based on the first author's personal communications with other atmospheric scientists who study convection, this is the most controversial aspect of the original Peters et al. (2019b) study that introduced the foundational theory for the V_{CR} and R relationship that was invoked in Part I. For instance, other atmospheric scientists have supposed that updrafts should be able to locally induce their own inflow that is of similar magnitude to that of V_{CR}, thus invalidating the proposed monotonic relationship between V_{IN} and V_{CR}. We address this possibility here.

c. After a cloud initially develops, how does it persist?

In the theoretical model, we assume that the cloud maintains a persistent updraft below the level of free convection (LFC) that continues to lift new inflowing air parcels into the cloud. Thus, if a cloud has a sufficient source of low-level V_{CR} and inflowing air that is conditionally unstable, it can maintain itself indefinitely. However, we did not explicitly characterize the dynamics responsible for the existence of this sub-LFC updraft in Part I. The present study will use the simulations to explore the pressure perturbation characteristics of the lower updraft, along with accelerations of air parcels as they approach the cloud updraft from below, to address this question.

The paper organization is as follows: section 2 outlines our numerical model design and our analysis strategies, sections 3–5 evaluates our hypotheses and research questions in the order they are listed above, and section 6 gives a summary, discussion, and conclusions.

2. Numerical model configuration

All 240-min-long simulations were run with Cloud Model 1 (CM1; Bryan and Fritsch 2002), version 20.3. Lateral boundary conditions (LBCs) were periodic, and top and bottom boundary conditions were free-slip. Our simulations featured two different domain sizes, with a smaller $25 \times 25 \times 25$ km^3 domain used in the unsheared simulations (following Morrison et al. 2021), and a larger $100 \times 100 \times 25$ km^3 domain used in the sheared simulations. A larger domain was needed in the sheared simulations to avoid interference with the DCI process by the lateral advection of convectively modified air across the periodic LBCs. To evaluate the sensitivity of our results to these differences in domain sizes, we reran several of the unsheared simulations with the $100 \times 100 \times 25$ km^3 domain, which produced similar cloud characteristics to that of the $25 \times 25 \times 25$ km^3 domain (not shown). The horizontal grid spacing was set to 100 m. Below 2 km, the vertical grid spacing was also 100 m. Above 2 km, we used a stretched vertical grid to save computational cost, with the vertical grid spacing gradually transitioning to 250 m by the domain top (stretch_z = 2, nz = 150, stretch_bot = 2000, stretch_top = 10 000 in the namelist.input file). There is ample evidence in past literature that this grid spacing is sufficient to explicitly resolve important updraft flow structures such as thermals (Lebo and Morrison 2015) and large turbulent eddies (Bryan and Fritsch 2002; Lin and Mitchell 2005), both of which play an important role in entrainment. Temporal integration used the time-splitting numerical integration scheme of Klemp and Wilhelmson (1978), with an adaptive time step. Microphysical processes were parameterized using the Morrison et al. (2009) double moment scheme with hail as the prognostic rimed ice species. All other simulation attributes aside from those that are explicitly discussed later in this section are set to the default values for this particular CM1 version, configured to LES mode.

TABLE 1. List of acronym, variable, and symbol definitions.

Acronym, variable, or symbol	Mathematical definition	Description in words
DCI		Deep convection initiation
RH		Relative humidity
R_0		Radius of subcloud (i.e., below cloud base) updraft that initiates cloud formation
s		Magnitude of vertical wind shear in environment surrounding cloud
R		Radius of cloud
R_G		Radius of the region of enhanced surface fluxes used to initiate a subcloud updraft
CAPE		Convective available potential energy
CIN		Convective inhibition
MUCAPE		Most unstable CAPE
MUCIN		Most unstable CIN
r_{PBL}		Water vapor mixing ratio in the near-ground portion of the initial model profile
ζ_{mean}		Average vertical vorticity in the 1–3-km layer
w_{mean}		Average vertical velocity in the 1–3-km layer
H	Section 3a	Updraft depth
$\Pi(x, y, z, t)$	Section 4	Exner function (nondimensional pressure)
$\Pi_0(z)$		Π of the reference state
Π'	$\Pi - \Pi_0$	Perturbation Π
Π_B	Eq. (13)	Buoyancy pressure (nondimensional)
Π_{DNL}	Eq. (15)	Nonlinear dynamic pressure (nondimensional)
Π_{DL}	Eq. (14)	Linear dynamic pressure (nondimensional)
Π_D		Total dynamic pressure (nondimensional)
Ψ		Passive tracer used as proxy for conditional instability
$\mathbb{R}$		Control volume radius in section 4
τ	Eq. (11)	Time scale of dissipation of Ψ in control volume
B	Section 5	Buoyancy
BPA	Eq. (16)	Vertical buoyancy pressure acceleration
EBPA	Eq. (16)	Vertical effective buoyancy pressure acceleration
NLPA	Eq. (16)	Vertical nonlinear dynamic pressure acceleration
LPA	Eq. (16)	Vertical linear dynamic pressure acceleration
DPA	Eq. (16)	Vertical total dynamic pressure acceleration
w_B	Section 5	w contribution from B
w_{BPA}	Section 5	w contribution from BPA
w_{EBPA}	Section 5	w contribution from EBPA
w_{LPA}	Section 5	w contribution from LPA
w_{NLPA}	Section 5	w contribution from NLPA
w_{DYN}	Section 5	w contribution from DPA
Variables related to ground-relative wind		
$\mathbf{V}(x, y, z, t)$		Full three-dimensional ground-relative wind vector
$\mathbf{V}_H(x, y, z, t)$		Full horizontal ground-relative wind vector
$\mathbf{V}_0(z)$		Ground-relative wind in reference state (set to initial model profile)
$\mathbf{V}'(x, y, z, t)$	$\mathbf{V} - \mathbf{V}_0$	Perturbation wind
$\mathbf{C}(t)$		Ground-relative cloud motion vector
Variables related to cloud-relative wind		
$\mathbf{V}_{\mathrm{CR}}(x, y, z, t)$	$\mathbf{V}_H - \mathbf{C}$	Cloud-relative component of full wind
$V_{\mathrm{CR}}(x, y, z, t)$	$\lvert\mathbf{V}_{\mathrm{CR}}\rvert$	Scalar magnitude of $\mathbf{V}_{\mathrm{CR}}$
$\mathbf{V}_{0,\mathrm{CR}}(z, t)$	$\mathbf{V}_0 - \mathbf{C}$	Cloud-relative component of reference state wind
$V_{0,\mathrm{CR}}(x, y, z, t)$	$\lvert\mathbf{V}_{0,\mathrm{CR}}\rvert$	Scalar magnitude of $\mathbf{V}_{0,\mathrm{CR}}$
$\mathbf{V}_{\mathrm{PG}}(x, y, z, t)$	Eq. (3)	Perturbation wind induced by horizontal pressure gradient accelerations
$\hat{\mathbf{d}}$	Eq. (4)	Unit vector pointing from parcel to updraft center
$V_{\mathrm{IN}}(x, y, z, t)$	$\hat{\mathbf{d}} \cdot \mathbf{V}_{\mathrm{CR}}$	Component of full cloud-relative wind in direction of updraft (i.e., inflow)
$V_{0,\mathrm{IN}}(z, t)$	$\hat{\mathbf{d}} \cdot \mathbf{V}_{0,\mathrm{CR}}$	Component of cloud-relative reference wind in direction of updraft
$V_{\mathrm{PG,IN}}(x, y, z, t)$	$\hat{\mathbf{d}} \cdot \mathbf{V}_{\mathrm{PG}}$	Component of pressure-induced wind in direction of updraft
$V_{\mathrm{PB,IN}}(x, y, z, t)$		Component of $V_{\mathrm{PG,IN}}$ driven by Π_B
$V_{\mathrm{PD,IN}}(x, y, z, t)$		Component of $V_{\mathrm{PG,IN}}$ driven by Π_D
$V_{\mathrm{PDNL,IN}}(x, y, z, t)$		Component of $V_{\mathrm{PG,IN}}$ driven by Π_{DNL}
$V_{\mathrm{PDL,IN}}(x, y, z, t)$		Component of $V_{\mathrm{PG,IN}}$ driven by Π_{DL}

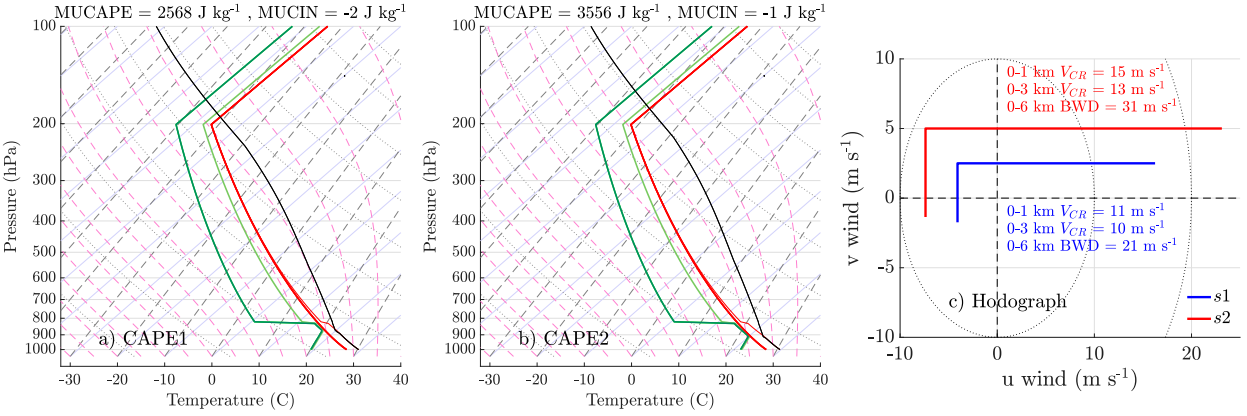

FIG. 1. (a),(b) Skew T–log$p$ plots of (a) CAPE1 and (b) CAPE2 temperature (°C, thick red line), virtual temperature (°C, thin red line), dewpoint temperature for RH = 40% (°C, dark green line) and RH = 80% (°C, light green line), and the density temperature (°C, thick black line) of a parcel lifted from the height of most unstable CAPE (MUCAPE), using the method described in Peters and Chavas (2021) and Peters et al. (2021). (c) Hodograph plot of the s1 (blue) and s2 (red) wind profiles. BWD = bulk wind difference.

The initial horizontally homogeneous environment and LBCs for simulations were created using the analytic equations from Weisman and Klemp (1982, hereafter WK82). The water vapor mixing ratio r_{PBL} in the near-surface part of this sounding, which modulates the CAPE of the sounding, was set to either 14 g kg^{-1} (Fig. 1a; hereafter CAPE1) or 16 g kg^{-1} (Fig. 1b; hereafter CAPE2). Motivated by the thermodynamic profiles used to evaluate the theoretical model in Part I, the RH in this profile was set to a constant value of either 40% (hereafter RH1) or 80% (hereafter RH2) above 1.5 km. Most unstable CAPE (MUCAPE) and convective inhibition (MUCIN) were 2568 and −2 J kg^{-1} for the RH1 CAPE1 profile, and 3556 and −1 J kg^{-1} for the RH1 CAPE2 profile, respectively. CAPE was roughly 100 J kg^{-1} smaller in the RH2 profiles than in the RH1 profiles due to slightly larger virtual temperatures T_v aloft in the case of the RH2 profiles. Note that the vertical discontinuity in RH in the RH1 profile is accompanied by an abrupt drop in T_v with height in this profile, resulting in a shallow dry absolutely unstable layer (DAUL). This is evident as the abrupt leftward jump in the thin red line at 850 hPa in Figs. 1a and 1b. This DAUL quickly mixed out during the model spinup periods (discussed below) without noteworthy changes to the bulk thermodynamic characteristics of the soundings.

Following Chavas and Dawson (2021), initial hodographs were shaped like a sideways "L" (Fig. 1c) with v wind linearly increasing with height and u wind held constant below 1 km, the u wind increasing linearly with height and the v wind held constant between 1 and 6 km, and a constant wind above 6 km. This profile is very similar in many respects to the iconic quarter-circle profile of Rotunno and Klemp (1982), featuring predominantly streamwise environmental horizontal vorticity below 1 km and predominately crosswise horizontal vorticity above 6 km (for a right-moving storm). We use this L-shaped vertical wind profile in lieu of the unidirectional profiles from Part I because the L-shaped profile more closely resembles that of real storm environments (Mitchell et al. 2004; Parker 2014). Bulk wind difference magnitudes s over the 0–6-km layer were either 0 m s^{-1} (hereafter s0), 21 m s^{-1} (hereafter s1), or 31 m s^{-1} (hereafter s2). Domain translation (imove = 1 in the namelist.input file) was set using a trial-and-error method to approximately center the active regions of deep convection within the domain. Note that the shear values used here are characteristic of typical supercell and squall-line environments. Thus, our results are most relevant to the genesis of these modes of convection.

We initialized convection using the surface-flux-driven technique following the cumulus congestus case from the 10th International Cloud Modeling Workshop (Shima and Grabowski 2020), similar to Moser and Lasher-Trapp (2017). For 1 h of the simulations, horizontally uniform surface potential temperature θ and water vapor mixing ratio fluxes of 0.03 K m^{-1} and 1×10^{-5} m s^{-1}, respectively, were applied to the lower boundary, allowing for the spinup of a turbulent PBL. Initial random potential temperature fluctuations with a maximum amplitude of 0.25 K were also added to the initial conditions throughout the domain to aid in the development of turbulence. Surface θ and water vapor mixing ratios only changed from their initial values by 0.1 K and 0.001 kg kg^{-1}, respectively, during this 1-h period. To give deep convection an opportunity to form during the 1–2-h time period of the simulations (hereafter "forcing period"), we added a Gaussian shaped region of enhanced fluxes atop these background fluxes in the center of the domain, with maximum flux magnitudes of 20 times the background value, which created a buoyant updraft within the subcloud layer. We varied the horizontal radii of influence R_G of this Gaussian flux region to control the initial subcloud updraft radius R_0. While R_G and R_0 were strongly correlated with one another (not shown), the scaling between these two parameters varied among the different initial model profiles because of the variations in wind, moisture, and temperature among these profiles. As a result, slightly different ranges of R_G were needed to achieve an approximately consistent range of R_0 for each initial model profile (see Table 2). This enhanced Gaussian flux region was turned off 2 h after the simulation start, leaving only the

TABLE 2. List of forcing radii R_G (km) corresponding to R indices in the names of simulations.

R index in simulation name	CAPE1 s0 R_G	CAPE2 s0 R_G	CAPE1 s1 R_G	CAPE2 s1 R_G	CAPE1 s2 R_G	CAPE2 s2 R_G
1	0.6	0.6	1.6	2.0	0.6	1.0
2	0.8	0.8	1.8	2.2	0.8	1.2
3	1.0	1.0	2.0	2.4	1.0	1.4
4	1.2	1.2	2.2	2.6	1.2	1.6
5	1.4	1.4	2.4	2.8	1.4	1.8
6	1.6	1.6	2.6	3.0	1.6	2.0
7	1.8	1.8	2.8	3.2	1.8	2.2
8	2.0	2.0	3.0	3.4	2.0	2.4
9	2.2	2.2	3.2	3.6	2.2	2.6
10	2.4	2.4	3.4	3.8	2.4	2.8
11	2.6	2.6	3.6	4.0	2.6	3.0
12	2.8	2.8	3.8	4.2	2.8	3.2
13	3.0	3.0	4.0	4.4	3.9	3.4

background uniform flux. Additional simulations with different domain sizes were run with a 250-m isotropic grid, warm bubble initialization, and open-radiative LBCs (not shown). This second set of simulations produced nearly identical results to the ones presented here, suggesting that our results were insensitive to the technique for DCI.

The combinations of r_{PBL}, RH, R_0, and s discussed in this section yielded a total of 120 simulations. Simulation names also reflect the relative size of their initial R_G (see Table 2). For instance, a simulation using RH of 40%, r_{PBL} of 14 g kg^{-1}, s of 21 m s^{-1}, and an R_G of 1.6 km is referred to as RH1 CAPE1 s1 R1.

To analyze parcel accelerations in later analysis, each simulation featured 50 000 forward trajectories initialized 90 min into each simulation, within the 0.5- to 12.5-km range in the x direction, the −10- to 15-km range in the y direction, and the 0.0- to 1.1-km range in the z direction, at intervals of 0.5, 0.25, and 0.1 km in the x, y, and z directions, respectively. Note that the horizontal center of the domain, and thus the center of each enhanced flux region, was located at $x = y = 0$ km. This region was intended to target parcels that would eventually become part of the updraft's low-level inflow. These trajectories were integrated using the built-in software in CM1, which features a second-order Runge–Kutta temporal integration scheme with a time step equal to the model integration time step. At each time step, model fields relevant to forthcoming analysis were interpolated onto the location of these trajectories.

3. Determining whether simulated updrafts behave like those in the theoretical model

Recall that the salient variables predicted by the theoretical model are V_{CR}, R, and H. In this section, we first outline our strategies for measuring the analogous quantities in the simulations. We then provide support for our hypothesis by showing that the behavior of these quantities in the theoretical model is qualitatively analogous to that of the simulations. To facilitate the comparison, we include plots from the theoretical model that are analogous to those shown from the simulations. To achieve the closest correspondence between theoretical model V_{CR} and R, and the simulations, we set $\sigma = 0.5$, $L = R/2$, and $\alpha = 0.2$ in our comparisons here, in lieu of $\sigma = 0.78$, $L = R/3$, and $\alpha = 0.3$ used in Part I. Changes in updraft evolution in the theoretical model also happened at roughly double the speed that they occurred in simulations, and we therefore multiplied the time step between each theoretical model integration by 2. None of these changes appreciably altered the qualitative behavior of the model. Rather, they resulted in subtle quantitative changes in R and H that made these quantities more comparable to simulated values.

The "raw" R and H values output from the theoretical model were then temporally interpolated onto one second intervals using a piecewise shape-preserving cubic interpolation (the "pchip" option in the MATLAB "interp1" function), with an assumed 0 initial value for all time series. This step did not qualitatively change any behavior or theoretical model interpretation. Rather, it yielded improved qualitative resemblance of the continuous output from the numerical simulations.

In the theoretical model plots included here, we use $s = 25$ m s^{-1} as an analogy to the s1 profile used in simulations, and $s = 35$ m s^{-1} as an analogy to the s2 profile used in simulations. These values of s were chosen as a compromise between the 0–6-km bulk wind differences of 21 and 31 m s^{-1} in the simulations, and the average shear magnitudes over the 0–6-km layer of 27 and 37 m s^{-1} (6 km)$^{-1}$, respectively. The thermodynamic profiles used in the theoretical model were identical to those used in the simulations. Finally, a range of R_0 in the theoretical model from 600 to 2400 m, at intervals of 200 m, are shown in plots. We caution the reader that a given R_0 from the simulations may not be directly comparable to the same R_0 in the theoretical model. Our qualitative verification of the theoretical model therefore focuses on whether the theoretical model replicates the general trends in cloud V_{CR}, R, and H in the simulations.

a. *Quantifying H in the simulations*

To obtain an estimate of H from the simulations, we began by computing the horizontal maximum of vertical velocity w at each height to obtain $w_{max}(z)$. In this computation, we ignored all points with a combined cloud water r_c and cloud

ice r_i mixing ratio less than 10^{-5} kg kg^{-1}. We then defined H as the highest instance of $w_{max}(z) > 3$ m s^{-1}.

b. Quantifying V_{CR} in the simulations

To estimate V_{CR} from the simulations, we first established time series of the simulated cloud motion vector **C**. At each output time, we calculated the vertical averages of w and vertical vorticity ζ between 1 and 3 km domain wide, to obtain w_{mean} and ζ_{mean}, respectively. We then set $w_{mean} = 0$ m s^{-1} at the grid points with $\zeta_{mean} < 0$ s^{-1}, to ensure that our analysis targeted the right-moving updrafts if storm splits occurred. A Gaussian shaped smoother with a radius of influence of 2.5 km was applied to w_{mean}, to obtain $w_{mean,s}$ (where the s subscript denotes "smoothed"). At each time, the center of the primary "updraft of interest" was assumed to correspond to the location of the domainwide maximum in $w_{mean,s}$. This procedure was applied to model data every 1 min, yielding a time series of storm locations $\mathbf{X}_s$. The storm motion components were subsequently defined as $\mathbf{C} \equiv d\mathbf{X}_s/dt$ using second-order centered-in-time finite differences, and linear extrapolation to obtain the first and last points along the time series. Note that the theoretical model assumes that local cloud-induced modifications to the $\mathbf{V}'(x, y, z, t)$ wind profile are small, and that the convectively unmodified horizontally uniform environmental profile $\mathbf{V}_0(z)$ dominates in determining V_{CR} (this assumption is validated in section 4 of the present study). Thus, to remain consistent with the theoretical model, much of our subsequent analysis of the simulations uses the quantity:

$$V_{0,CR}(z,t) = |\mathbf{V}_{0,CR}| = |\mathbf{V}_0 - \mathbf{C}|, \quad (1)$$

where $\mathbf{V}_0(z)$ is assumed to correspond to the initial model profile. In a manner consistent with the theoretical model, time series of $V_{0,CR}$ were computed by averaging $V_{0,CR}(z)$ from the lowest model level to the height of the vertical maximum in $w_{max}(z)$, which is consistent with the "deep inflow hypothesis" of Schiro et al. (2018). Results were insensitive to variations in the depth of the layer used to average $V_{0,CR}(z)$.

Occasionally the tracking procedure would jump between adjacent clouds resulting in transient instances of spuriously large $V_{0,CR}$. To remove these instances, we first subtracted the 50-min running median from each $V_{0,CR}$ time series, and defined points as outliers in the resulting time series if their scaled median absolute deviation exceeded 3. We then replaced outliers by linearly interpolating onto outlier time steps from temporally adjacent no-outlier points. The resulting $V_{0,CR}$ time series was then smoothed with a Gaussian filter with a radius of influence of 10 min.

c. Quantifying R in the simulations

Updraft area A was first defined as the largest continuous area of unsmoothed $w_{mean} > 3$ m s^{-1} that contained $\mathbf{X}_s$ at a given time. To facilitate the comparison between simulated updrafts, which were not necessarily circular, and the theoretical model, which assumed circular updrafts and therefore relied heavily on the R of the updraft, we computed the radius of a circle with equivalent area to A, such that $R \equiv \sqrt{A/\pi}$ in the simulations.

d. Evidence for the progressive rooting hypothesis in the simulations

We first examine the unsheared s0 simulations to establish a basis of comparison for our later analysis of sheared simulations. Note that we excluded an analysis of $V_{0,CR}$ in the s0 simulations because this quantity is poorly defined in the absence of shear. Time series of R (Figs. 2a,c and 3a,c) and H (Figs. 2b,d and 3b,d) show relatively rapid increases in these values to their respective peaks shortly after the end of the forcing periods, and then commensurately quick declines after peak values, with convective lifespans lasting approximately 1 h. Furthermore, peak R and H values were generally dependent on R_0 (Figs. 2a–d and 3a–d). This correspondence between R_0, and R and H is also present in the theoretical model (Figs. 4a–d and 5a–d). In fact, both the simulations (blue lines in Figs. 6a–d) and theoretical model (blue lines in Figs. 7a–d) suggest a positive scaling between R_0, and R and H, which is consistent with the results of Morrison et al. (2021). Interestingly the theoretical model shows a larger difference in H between the RH1 and RH2 profiles (Figs. 7a–d) than was present in the simulations (Figs. 6a–d). Moist thermals rising in unsheared background environments actually do experience nonzero aerodynamic drag in an analogous manner to sheared moist thermals (albeit to a lesser extent), because of the turbulence-induced lateral movement of thermals as they rise (see Fig. 8 in Peters et al. 2019a), but this is neglected in the theoretical model. This possibly explains the discrepancy in theoretical versus simulated updraft depths in the RH1 versus RH2 s0 simulations. Increasing the shear to moderate levels (s1) with RH1 had only subtle effects on the evolution of R and H. Values of R (Figs. 2e and 3e), H (Figs. 2f and 3f), and $V_{0,CR}$ (Figs. 2g and 3g) once again peaked just after the end of the forcing period, and but more gradually declined thereafter than in the case of the s0 simulations reflecting more prolonged convective activity. Peak values of H were also somewhat smaller in the s1 simulations than in the s0 simulations (cf. Figs. 3f and 2f to Figs. 3b,d and 2b,d), hinting at an enhanced shear suppression effect in s1, relative to s0, simulations. Like in the case of the s0 simulations, peak values of H (red dashed lines in Figs. 6a,c) and R (red dashed lines in Figs. 6b,d) showed a positive scaling with R_0, suggesting a strong influence of the subcloud updraft size on the characteristics of the resulting cloud. While several simulations produced updrafts that approached the depth of the troposphere (which was 12 km), and would therefore be considered by many as "deep," these deep updrafts did not last very long after the end of the forcing period. The aforementioned behaviors are qualitatively mimicked by the theoretical model in time series of R (Figs. 4e and 5e), H (Figs. 4f and 5f), and $V_{0,CR}$ (Figs. 4g and 5g), and in the dependencies of peak R and H on R_0 in the theoretical model (Figs. 7a–d).

The behavior in the RH2 s1 simulations (Figs. 2h–j and 3h–j) was markedly different than that of the RH1 s1, and s0

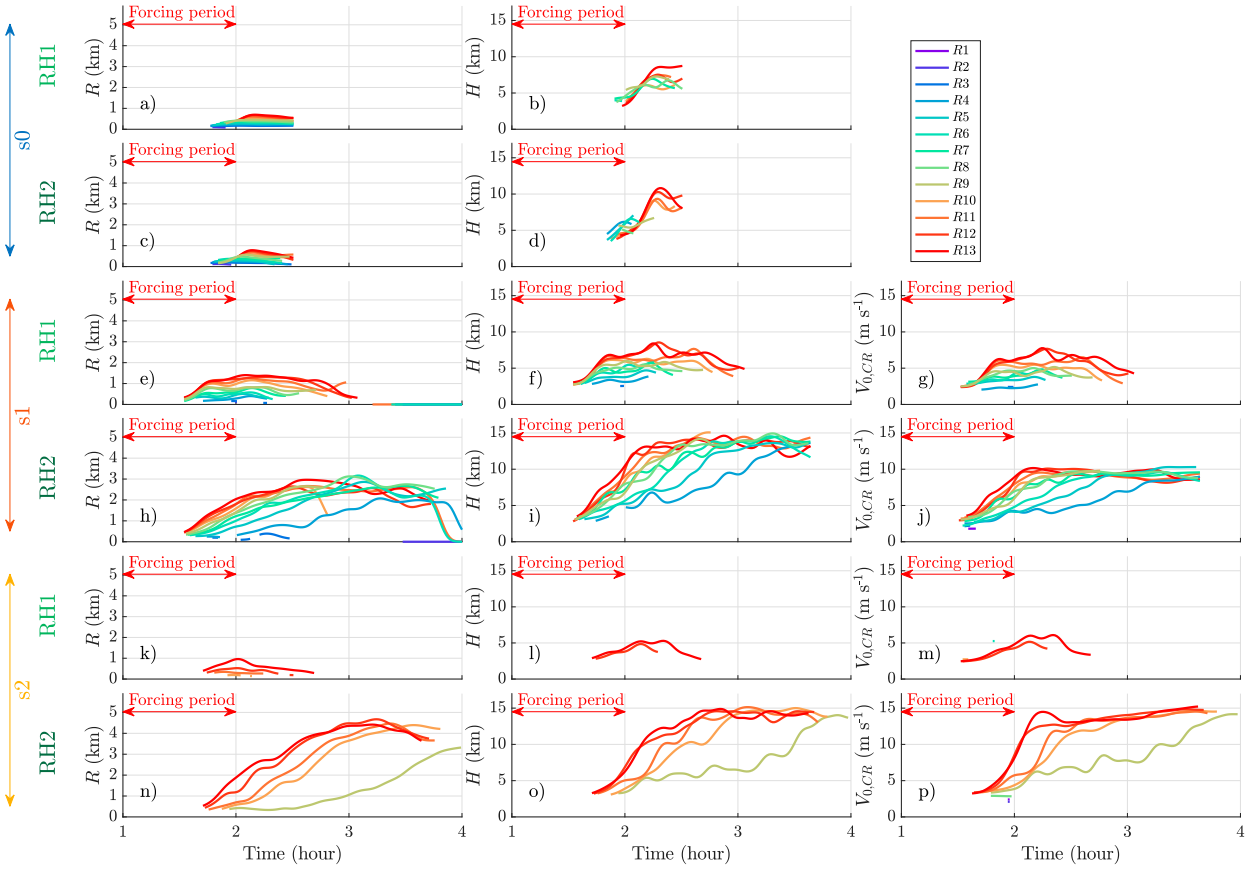

FIG. 2. Time series from the CAPE1 simulations of (left) R (km), (center) H (km), and (right) $V_{0,\mathrm{CR}}$ (m s^{-1}). Colors correspond to various forcing radii R_G and thus R_0, as indicated by the R indices in the upper-right legend (R_G values for all runs are listed in Table 2). (a),(b) The RH1 s0 simulations. (c),(d) The RH2 s0 simulations. (e)–(g) The RH1 s1 simulations, (h)–(j) the RH2 s1 simulations, (k)–(m) the RH1 s2 simulations, and (n)–(p) the RH2 s2 simulations. The forcing period is annotated with a red double-ended arrow.

simulations. While the RH2 s1 simulations with the smallest R_0 only produced very shallow cumulus whose updrafts were not picked up by our tracking algorithm, R, H, and $V_{0,\mathrm{CR}}$ in most simulations gradually increased to steady values. Furthermore, peak H and R no longer scaled with R_0 in these simulations (solid red lines in Figs. 6a–d), suggesting that factors other than the initial subcloud updraft width were controlling these cloud characteristics. This loss of dependency of R and H on R_0 is replicated by the theoretical model (Figs. 4h–j and 5h–j; solid red lines in Figs. 7a–d).

Increasing the shear to the largest magnitude (s2) produced noticeable differences in the behavior of the simulations with the RH1 profile, when compared to s0 and s1 simulations with RH1. For instance, the RH1 CAPE1 s2 struggled to produce any convection at all (Figs. 2k–m), with H (Fig. 2l) far smaller than in the s0 (Figs. 2b,d) and s1 (Figs. 2f,i) simulations. In fact, among the RH1 s2 simulations, most R_0 failed to produce sufficiently strong updrafts for our tracking algorithm to identify. In the RH1 CAPE2 s2 simulations with small R_0 (R1–7; Fig. 3l), a similar behavior occurred to that of the RH1 CAPE1 s2 simulations, with peak R (Fig. 3k) and H (Fig. 3l) occurring during or shortly after the forcing period, and a quick decay of updrafts after the forcing ceased. Like in the case of all other simulations that failed to produce steady updrafts, R and H scaled positively with R_0 in the RH1 CAPE1 s2 simulations, and RH1 CAPE2 s2 simulations with small R_0 (yellow dashed lines in Figs. 6a–d), and similar behavior is evident in the theoretical model (Figs. 4k–m and 5k–m; yellow dashed lines in Figs. 7a–d).

In contrast with the RH1 CAPE2 s2 simulations with small R_0, in the RH1 CAPE2 s2 simulations with large R_0 (R8–13), R (Fig. 3k), H (Fig. 3l), and $V_{0,\mathrm{CR}}$ (Fig. 3m) increased to steady common values, where they generally remained until the end of the simulations, mimicking what occurred in the RH2 s1 simulations (Figs. 2h–j and 3h–j). Values of H and R no longer scaled with R_0 in the RH1 CAPE2 s2 simulations with large R_0 (yellow dashed lines in Figs. 6a–d), with all R instead evolving toward a common steady value irrespective of R_0. The theoretical model produces remarkably similar behavior (Figs. 5k–m; yellow dashed lines in Figs. 7a–d), wherein updrafts with an $R_0 < 1.65$ km decay quickly and updrafts with an $R_0 > 1.65$ km evolve toward a steady R.

As was the case in the s1 simulations, initial convection evolved into quasi-steady updrafts in nearly all of the RH2

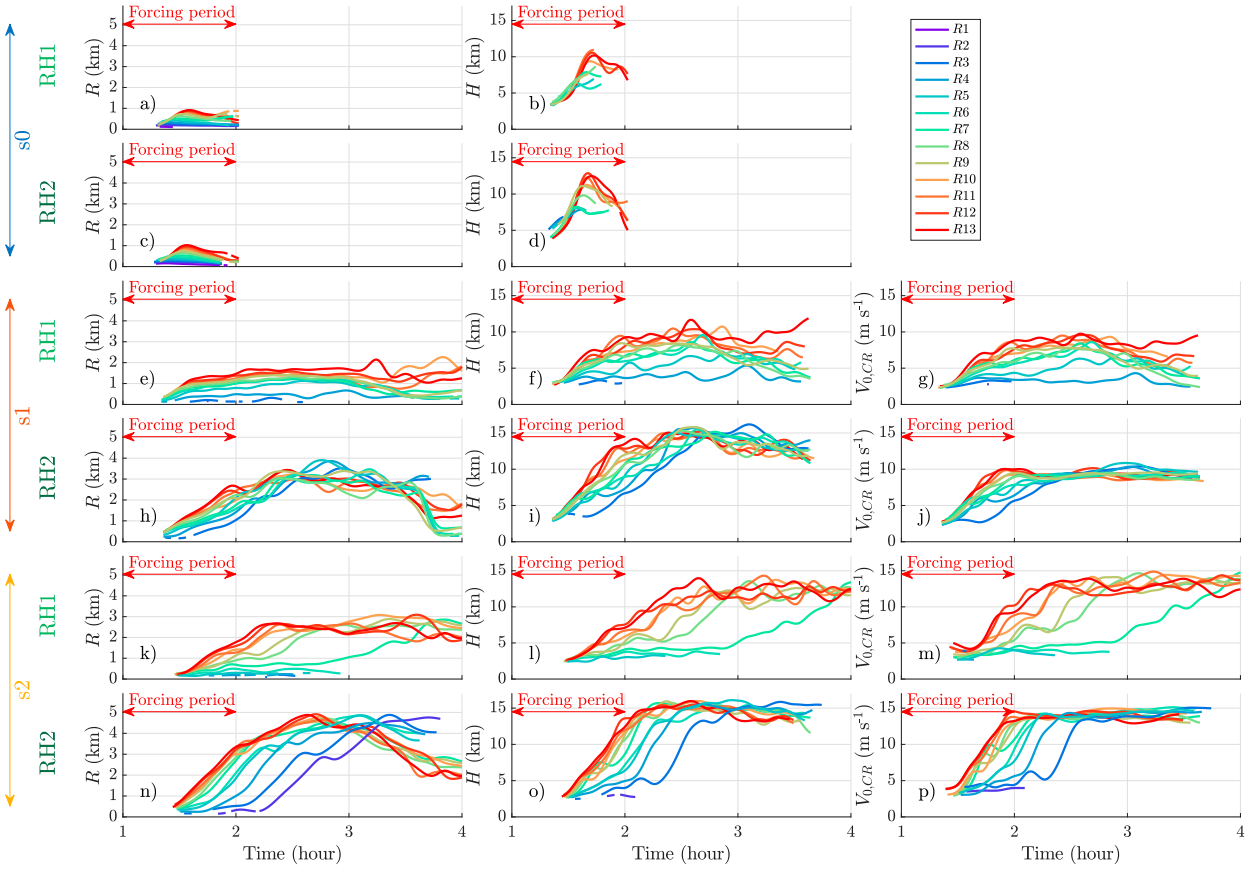

FIG. 3. As in Fig. 2, but for the CAPE2 simulations.

CAPE2 s2 simulations (Figs. 3n–p), with peak R and H showing little correspondence with R_0 (yellow solid lines in Figs. 6a–d). The theoretical model, once again, shows similar behavior (Figs. 5n–p; yellow solid lines in Figs. 7a–d). Interestingly, while steady updrafts did occur in the RH2 CAPE1 s2 simulations, they only did for the largest R_0 values (Figs. 2n–p). This marks a qualitative departure of the theoretical model from the simulations, wherein the theoretical model suggests that nearly all R_0 should evolve toward steady updrafts (Figs. 4n–p). A possible reason for this discrepancy between the theoretical model and the simulations is our neglect of CIN in the theoretical model, which was nonzero in the CAPE1 sounding and slightly larger in magnitude than that of the CAPE2 sounding.

Time–height diagrams of the horizontal domain maximum in w (Fig. 8) show that simulated updrafts were thermal-like during their nascent stages, composed of series of quasi-discrete updraft pulses (evident as the nearly vertical "stripes" of enhanced w in the figure). Though we only show a small subset of the simulations as an example here, this thermal-like behavior during nascent cloud states was ubiquitous among all simulations. Increases in updraft depth among simulations that achieved quasi-steady updrafts (Figs. 8c–f) occurred as stepwise increases in the cloud termination heights with time, which is consistent with the assumptions in the theoretical model (see section 3b in Part I).

In general, several key aspects of the simulations are captured by the theoretical model. First, increases or decreases in R with time are accompanied by commensurate increases or decreases in $V_{0,\mathrm{CR}}$ in the simulations and theoretical model, which is the central assumption in the hypothesis. This relationship is corroborated by a strong correlation between R and $V_{0,\mathrm{CR}}$ during the nascent (Fig. 6e) and mature (Fig. 6f) stages of cloud evolution among all simulations. Note that similar dependencies of R on $V_{0,\mathrm{CR}}$ are depicted in the theoretical model (Figs. 7e,f).

Second, general dependencies in the theoretical model of whether updrafts were steady or transient, on R_0, s, RH, and CAPE, were consistent with the simulations. For instance, R_0 primarily determined whether steady updrafts occurred for a given s, RH, and CAPE. Steady updrafts are generally more likely for a given R_0 when s, RH, and CAPE are large, than when these quantities are comparatively small.

Finally, there is a bifurcation in simulated and theoretical updraft outcomes, whereby initial updrafts that exceed critical thresholds for these environmental attributes grow to common steady-state R and H, whereas initial updrafts that do not exceed these critical thresholds do not persist to the end of the simulation. Updraft attributes in the simulations that achieved a steady state were generally uncorrelated with the width of the initial subcloud updraft R_0 (i.e., updraft attributes

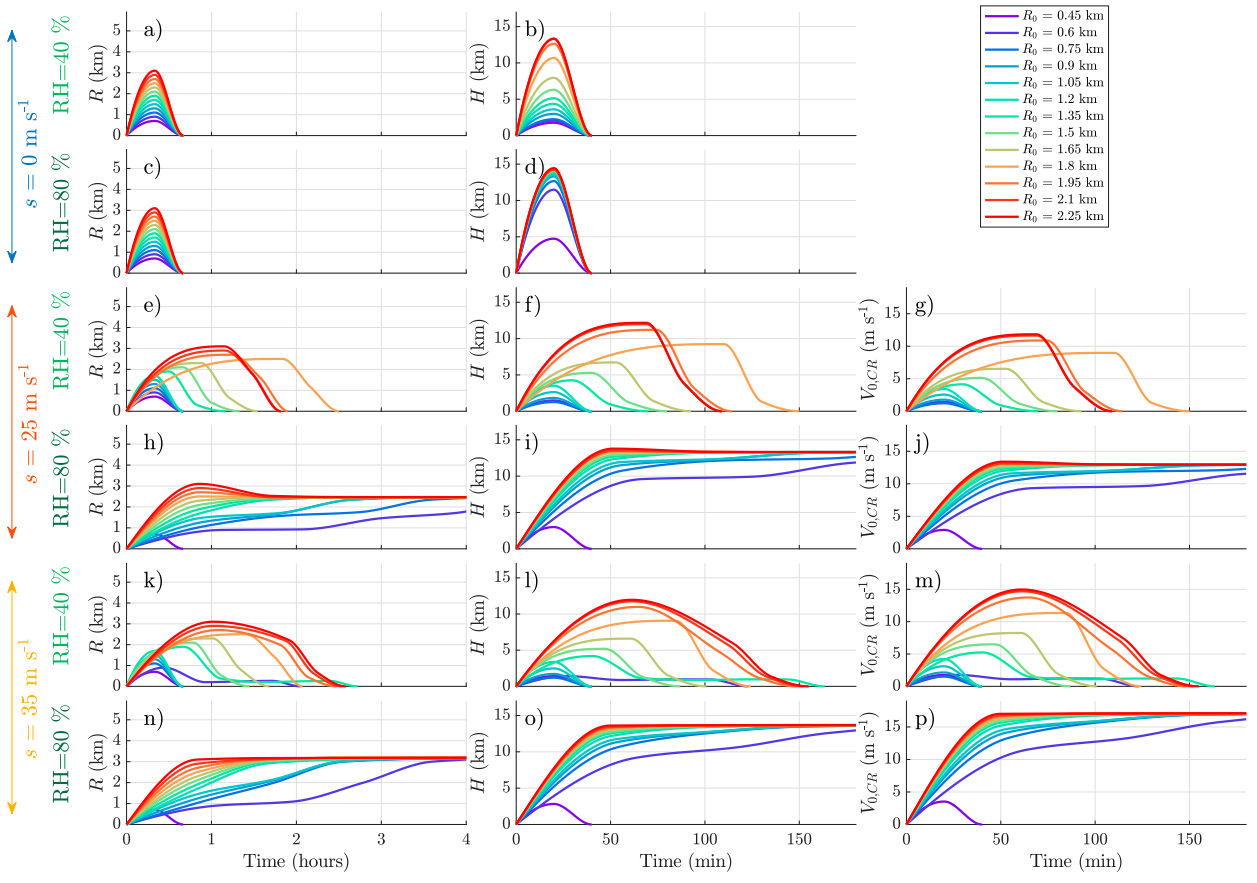

FIG. 4. As in Fig. 2, but for the theoretical model, and for the parameter values indicated in the figure labels.

heavily dependent on environmental variables, such as s), whereas updraft attributes in the simulations that did not achieve a steady state were strongly dependent on R_0.

e. *Evidence for the shear suppression effect in the simulations*

Next, we want to determine whether our representation of the shear suppression effect in the theoretical model is consistent with how shear suppresses cloud growth in the simulations. This comparison is somewhat challenging in the simulations where steady-state updrafts developed, given that the progressive deepening of clouds counteracts and conceals the shear suppression effect. We therefore focus our analysis on the simulations wherein steady updrafts did not develop, and wherein progressive rooting did not occur.

To evaluate the theoretical model, we determine whether differences in H among the s0, s1, and s2 simulations are consistent with the analogous differences in the H predicted by the theoretical model for $s = 0$ m s^{-1} (6 km)$^{-1}$, $s = 25$ m s^{-1} (6 km)$^{-1}$, and $s = 35$ m s^{-1} (6 km)$^{-1}$ (Fig. 9). As is predicted by theory (i.e., the blue curve is to the left of the red and yellow curves in Fig. 9a), s0 simulations generally produced deeper clouds (larger H) for a given R than the s1 and s2 simulations in the environments with low RH (i.e., the blue dots are to the left of the red and yellow dots in Fig. 9). Furthermore, differences in H for a given R among the s0, and s1 and s2 simulations were somewhat comparable to the analogous differences portrayed in the theoretical model (Fig. 9). Finally, differences between the H at a given R in the s1 and s2 simulations were virtually nonexistent (i.e., the red and yellow dots occupy similar regions in Fig. 9), which is again consistent with what is portrayed in theory (i.e., the red and yellow curves are close to one another in Fig. 9). These favorable comparisons suggest that the theoretical model portrays the shear suppression effect in a qualitatively realistic manner. A similar comparison in the higher RH simulations was not possible, given that all of the s1 and s2 simulations produced steady updrafts (Fig. 9b).

4. How valid is the assumption that V_{IN} is exclusively determined by environmental cloud-relative flow (V_{CR})?

To address this question, we begin by revisiting the link between V_{IN} and updraft R. Recall that inflow is defined as the speed of air as it moves inward across the updraft periphery, relative to the cloud motion. Mass continuity dictates that upward mass flux in an updraft must be balanced by lateral inward mass flux below. For an idealized cylindrical updraft, the vertical mass flux is determined by R and w, and the

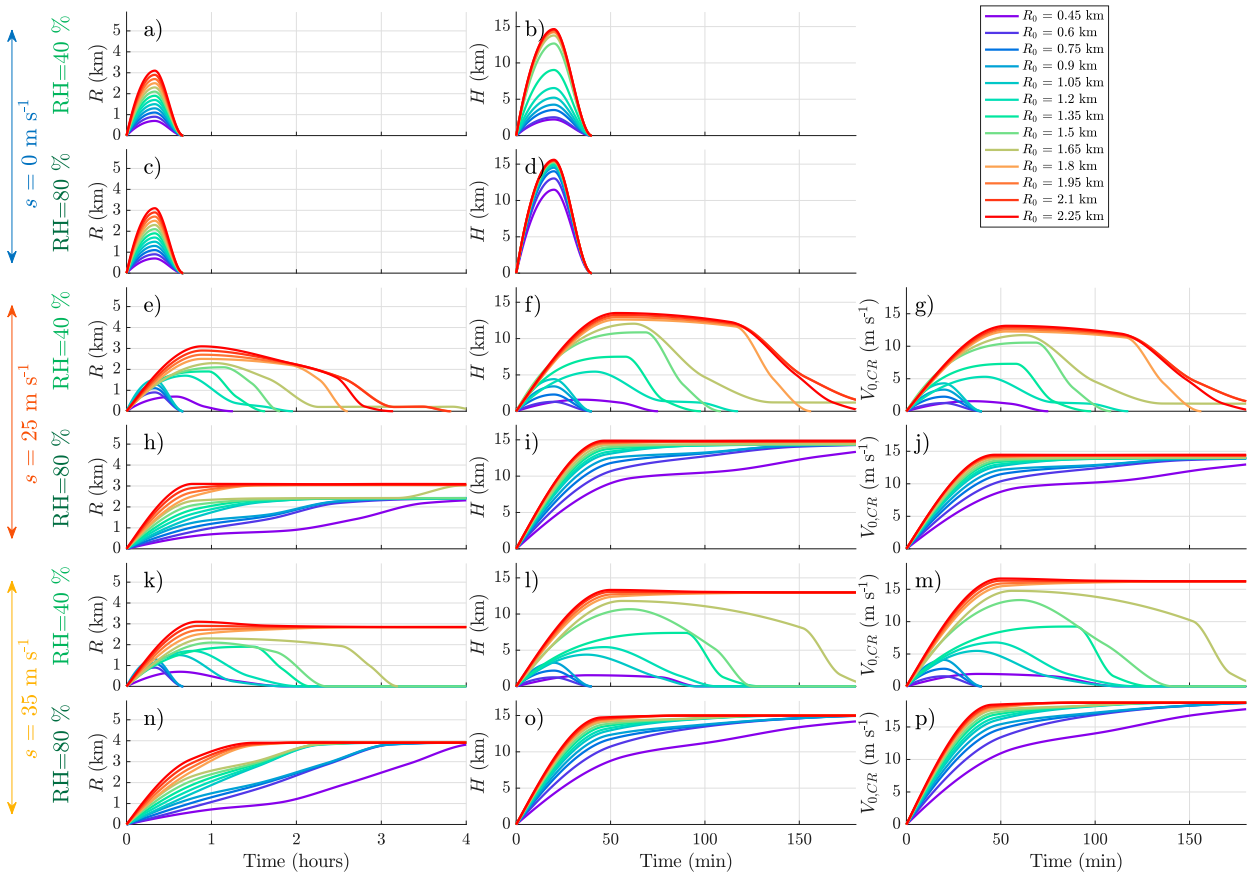

FIG. 5. As in Fig. 4, but for CAPE2.

horizontal mass flux is determined by R and V_{IN}, implying a connection between V_{IN} and R. In fact, using simplifications of the equations of motion, Peters et al. (2019b) showed that this mass continuity principle leads to a positive and nearly linear relationship between V_{IN} and R, meaning that wider updrafts should have faster inflow than narrower updrafts. This theoretical relationship, which is consistent with intuition, has been confirmed by numerous numerical modeling simulations (e.g., Peters et al. 2019b, 2020a,b).

In previous work (including Part I), we assumed that $V_{0,\mathrm{CR}}$—the cloud relative wind of the background environment—determines V_{IN}. This assumption was convenient, because it allowed us to connect $V_{0,\mathrm{CR}}$, which is readily estimated from a single profile of the background environment, to R. The connection was supported by strong correlations between $V_{0,\mathrm{CR}}$ and V_{IN} in Peters et al. (2019b), and between $V_{0,\mathrm{CR}}$ and R in the present study and previously in Warren et al. (2017). So this connection appears to be valid, albeit for reasons that have not yet been clarified. Hence, we investigate the dynamics responsible for the aforementioned relationships in this section.

We begin our investigation with the inviscid Lagrangian tendency equation for the horizontal wind vector $\mathbf{V}_H$, which may be written as

$$\frac{d\mathbf{V}_H}{dt} = -c_{pd}\theta_\rho \nabla_H \Pi', \tag{2}$$

where $\Pi \equiv (p/p_{\mathrm{ref}})^{R_d/c_{pd}}$ is the Exner function, $\Pi' = \Pi - \Pi_0$, Π_0 represents the initial model profile in the simulations, which is used here in lieu of p to maintain consistency with the CM1 source code, $\theta_\rho \equiv \theta\left[1 + (R_v/R_d)r_v/(1 + r_t)\right]$ is density potential temperature, $\theta \equiv T/\Pi$ is potential temperature, T is temperature, R_v and R_d are the specific gas constants of water vapor and dry air, respectively, c_{pd} is the specific heat capacity of dry air, r_v is the water vapor mixing ratio, and r_t is the total water mixing ratio. While in CM1 $\mathbf{V}_0$ is simply set to the initial model profile, in the real world one may consider $\mathbf{V}_0$ to represent a sounding taken within a cloud's inflow, and sufficiently far from the cloud to avoid sampling local cloud modifications to the wind field.

Temporally integrating Eq. (2) from some initial time t_0 when $\mathbf{V}_H = \mathbf{V}_0$ to some arbitrary later time t and subtracting the cloud motion vector $\mathbf{C}$ from each side gives

$$\underbrace{\mathbf{V}_{\mathrm{CR}}}_{\substack{\text{Total cloud-}\\\text{relative wind}}} = \underbrace{\mathbf{V}_{0,\mathrm{CR}}}_{\substack{\text{Background cloud-}\\\text{relative wind}}} - \underbrace{\int_{t^*=t_0}^{t^*=t_{\mathrm{IN}}} c_{pd}\theta_\rho \nabla_H \Pi' dt^*}_{\substack{\mathbf{V}_{\mathrm{PG}}\text{, locally-}\\\text{induced wind}}}. \tag{3}$$

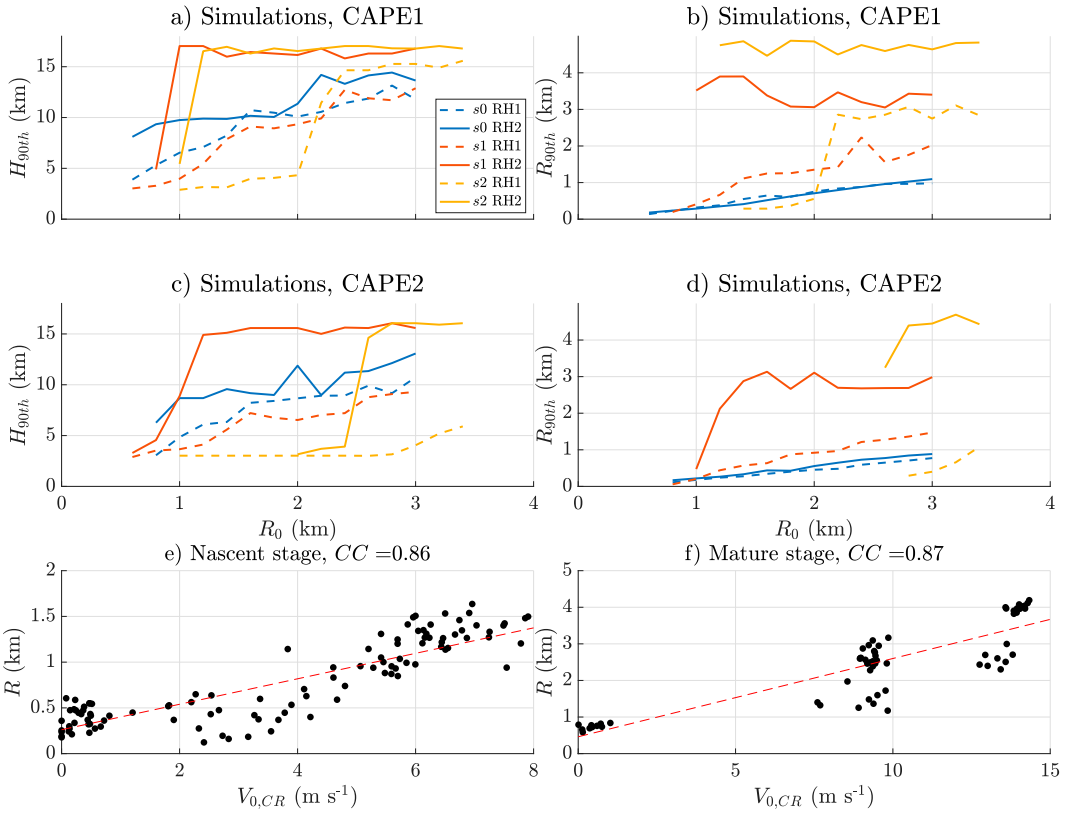

FIG. 6. (a)–(d) R_0 (km, x axis, also see Table 2) vs the 90th percentile of H (H_{90th}, km, y axis) from the simulations. Dashed lines correspond to RH1, whereas solid lines correspond to RH2. Blue, red, and yellow correspond to s0, s1, and s2 simulations, respectively. (e),(f) Scatterplots of $V_{0,CR}$ (m s^{-1}, x axis) vs R (km, y axis) from all simulations: (e) Averaged during the nascent stage between the first instance of maximum domain w greater than 10 m s^{-1}, and prior to maximum domain w exceeding 40 m s^{-1}; (f) Averaged during the mature stage, after maximum domain w exceeding 40 m s^{-1}. CC = correlation coefficient.

Using this equation, we may represent the horizontal cloud-relative wind at any time t as the sum of the cloud-relative wind of the background environment, and the cloud-relative wind resulting from storm-induced pressure accelerations. We define the direction between a parcel (subscript "par") and the updraft (subscript "ud") at any given time as

$$\hat{\mathbf{d}} \equiv \left[(x_{\text{par}} - x_{\text{ud}})^2 + (y_{\text{par}} - y_{\text{ud}})^2\right]^{-1/2}\left[(x_{\text{par}} - x_{\text{ud}})\hat{\mathbf{i}} + (y_{\text{par}} - y_{\text{ud}})\hat{\mathbf{j}}\right]. \quad (4)$$

Forming the inner product of $\hat{\mathbf{d}}$ with Eq. (3) yields

$$V_{\text{IN}} = V_{0,\text{IN}} + V_{\text{PG,IN}}, \quad (5)$$

where $V_{\text{IN}} \equiv \hat{\mathbf{d}} \cdot \mathbf{V}_{H,\text{CR}}(t)$ is the total inflow at time t, $V_{0,\text{IN}} \equiv \hat{\mathbf{d}} \cdot \mathbf{V}_{0,\text{CR}}$ is the component of inflow due to the background environmental wind, and $V_{\text{PG,IN}} \equiv -\hat{\mathbf{d}} \cdot \int_{t^*=t_0}^{t^*=t_{\text{IN}}} c_{\text{pd}}\theta_\rho \nabla_H \Pi' dt^*$ is the storm-induced pressure component of inflow.

Part I assumes that $V_{\text{IN}}(t) \approx V_{0,\text{IN}}$, and hence $V_{\text{PG,IN}}/V_{0,\text{IN}} \ll 1$. To validate this assumption in the simulations, we examine the ratio of $r_{\text{PG}} = V_{\text{PG,IN}}/V_{0,\text{IN}}$ along all s1 and s2 trajectories as they approach the updraft (s0 trajectories are excluded from this analysis). This ratio was, perhaps surprisingly, small during the nascent stages of updrafts (Figs. 10a,b), with $|r_{\text{PG}}| < 0.2$ for 80% of trajectories beyond ≈6 km, and $|r_{\text{PG}}| < 0.2$ away from the updraft edge and the sign of r_{PG} weakly positive, indicating that more parcels were accelerated toward the updraft than away from it. Further, only 20% of parcels experienced a $r_{\text{PG}} > 0.2$ prior to parcels reaching the updraft edge. This suggests that, while nascent updrafts do induce inward accelerations, the resulting enhancement to inflow is small relative to the speed of the background cloud-relative wind. Interestingly, r_{PG} abruptly became larger in magnitude and negative within 1 km of the updraft edge, suggesting a strong deceleration of parcels as they neared updraft entry. The reasons for this behavior are discussed later in this section.

As a sanity check on the accuracy of our calculations, we include plots of $(V_{\text{IN}} - V_{0,\text{IN}})/V_{0,\text{IN}}$ (Fig. 10a), which is the ratio of storm-induced inflow to environmental inflow computed with wind components directly interpolated onto trajectory paths, to $V_{\text{PG,IN}}/V_{0,\text{IN}}$ (Fig. 10b), which is the ratio of storm-induced inflow

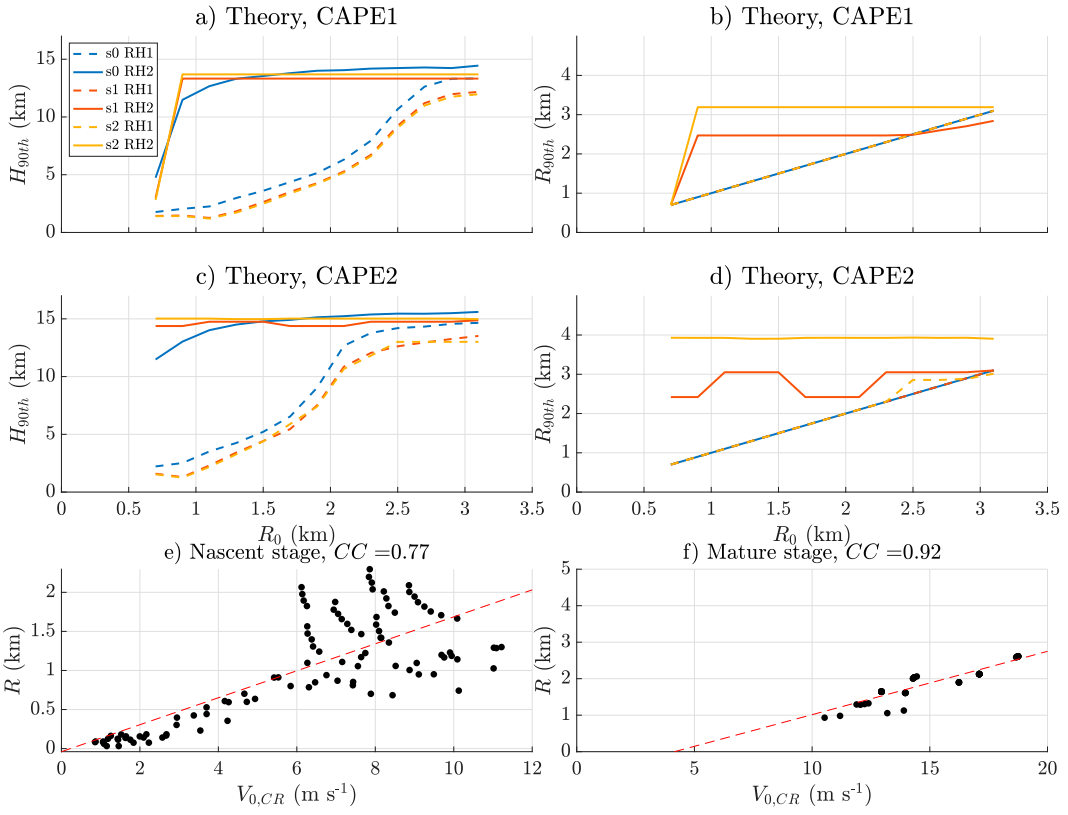

FIG. 7. As in Fig. 6, but for the theoretical model.

computed via the integration of pressure accelerations along trajectory paths to the environmental inflow. These quantities are nearly identical, which suggests that our temporal integrations of the pressure accelerations along trajectory paths were accurate, and that pressure accelerations were the primary accelerations acting upon parcels as they approached updrafts (as opposed to accelerations from subgrid diffusion).

These results suggest that the "radius of influence" of updrafts on their local winds was generally similar to the R of updrafts themselves, which ranged from 0.5 to 2 km during the nascent sages of cloud development (Figs. 2a,c,e,h,k,n and 3a,c,e,h,k,n). This result is quite consistent with in situ observations near supercells during the Mesoscale Predictability Experiment (Weisman et al. 2015), which showed that

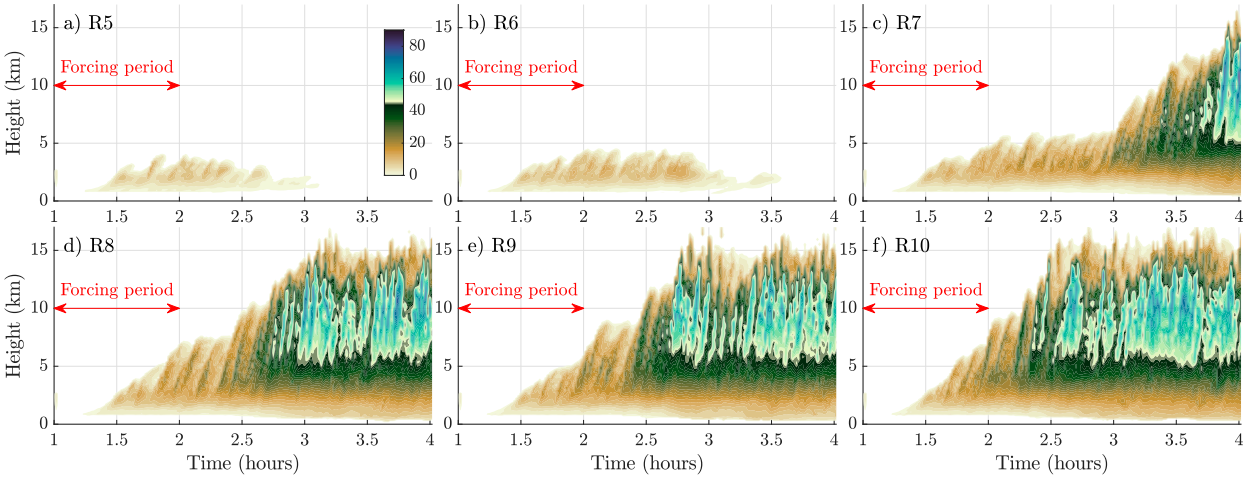

FIG. 8. Time (h, x axis) vs height (km, y axis) diagrams of the horizontal maximum in w (m s^{-1}, color shading) for selected RH1 CAPE2 s2 simulations (see panel labels for R_0, also see Table 2). The forcing period is annotated with a red double-ended arrow.

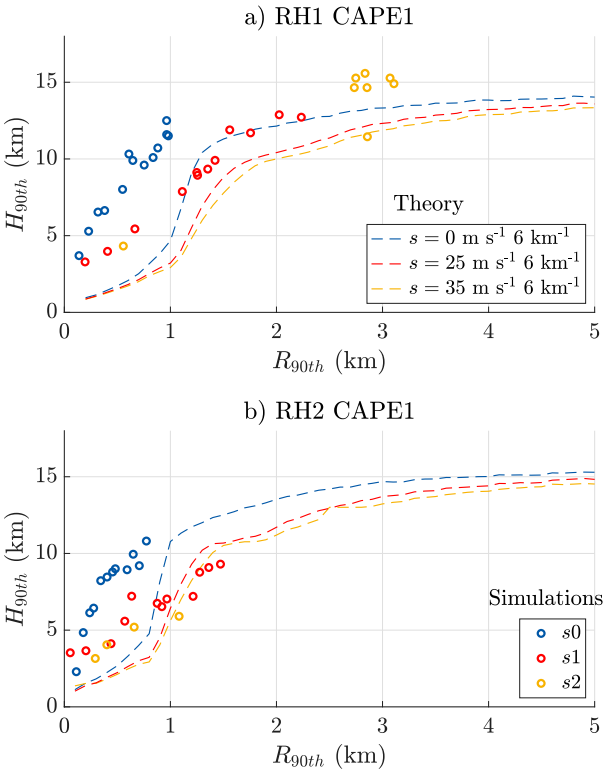

FIG. 9. Comparisons of R (km) and H (km) from theory (dashed lines) and the simulations (dots). Theoretical curves trace 90th percentile of R (km, x axis) vs the 90th percentile of H (km, y axis) among theoretical model time steps. Data points from simulations show the 90th percentile of R (km, x axis) vs the 90th percentile of H (km, y axis) among 1-min model outputs. Blue: s0 simulations and $s = 0$ m s^{-1} (6 km)$^{-1}$ in the theoretical solution. Red: s1 simulations and $s = 25$ m s^{-1} (6 km)$^{-1}$ in the theoretical solution. Yellow: s2 simulations and $s = 35$ m s^{-1} (6 km)$^{-1}$ in the theoretical solution. (a) The RH1 CAPE1 simulations. (b) The RH2 CAPE1 simulations.

supercells' influence on their environment is generally limited to distances from the updraft that are similar to the updraft scale itself (Trapp and Woznicki 2017). Indeed, composites of $\mathbf{V}_{CR}$ (the total cloud relative wind field) at 1.05 km AGL shows generally southeasterly cloud-relative flow everywhere in the vicinity of the updraft, with a local maximum in speed along the eastern updraft flank, and a local minimum along the western flank (Fig. 11a). The magnitude of $\mathbf{V}'$ was generally maximized along the western updraft flank, downstream of the primary direction of inflow, and was generally small outside the immediate vicinity of updraft (Fig. 11b). The modest acceleration of parcels approaching the updraft from the southeast and deceleration of parcels to the west and northwest is consistent with the presence of negative Π' along the eastern updraft flank (Fig. 11c), which would have accelerated parcels approaching the updraft from the east and decelerated westward moving parcels to the updraft's west. These patterns qualitatively confirm the idea that locally induced inflow was confined to the region close to the updraft, especially in the primary direction of inflow. Further, the pronounced deceleration of flow on the downstream (i.e., western) flank of the updraft is consistent with the conceptual framework of the theoretical model, which asserts that the updraft "captures" a substantial fraction of inflow, leaving a wake of slower moving air on its downstream side.

Do these analyses support the assertion that $|\mathbf{V}_{CR}| \gg |\mathbf{V}_{PG}|$ in the theoretical model? Not definitively, yet. We have shown that $|\mathbf{V}_{PG}|$ is only substantial in the immediate vicinity of the updraft, roughly within a distance of R of the updraft edge. Beyond this distance, $|\mathbf{V}_{PG}|$ becomes negligibly small. Thus, the updrafts in our simulations do not inwardly accelerate air parcels from far-reaching areas; they only do so to parcels that are already close to the updraft.

Consistent with the notion that $|\mathbf{V}_{CR}| \gg |\mathbf{V}_{PG}|$, we introduce the idea that $|\mathbf{V}_{CR}|$ delivers conditionally unstable air to the updraft's close proximity. From there, the updraft's own horizontal accelerations (i.e., $\mathbf{V}_{PG}$) will help to ingest these air parcels. Thus, we propose that without sufficient $|\mathbf{V}_{CR}|$, an updraft may quickly exhaust the conditionally unstable air within its vicinity faster than conditionally unstable air can be resupplied by the large-scale environment, leading to updraft demise. The aforementioned idea may explain why $|\mathbf{V}_{CR}|$ is a skillful predictor of updraft longevity, besides its connection with R.

To support this idea with theoretical arguments, we will assume that conditional instability behaves like a passive tracer ψ, where $\psi = 1$ implies conditionally unstable flow and $\psi = 0$ implies a lack of conditional instability. This assumption is justified by the link between conditional instability and (approximately) conserved thermodynamic variables such as moist static energy MSE and moist entropy s_m, which themselves behave in a similar manner to a passive tracer in the absence of significant diabatic enthalpy and entropy sources/sinks. Note that we are implicitly neglecting the influences of processes occurring above a given parcel on that parcel's conditional instability, such as warming/cooling aloft and the associated effect on the buoyancy of a lifted parcel.

We restrict ourselves to the lowest few kilometers of the troposphere where convective instability typically resides, and where the Boussinesq approximation is valid. The Boussinesq cylindrical governing equation for ψ may be written in flux form as

$$\frac{\partial \psi}{\partial t} + \frac{1}{r}\frac{\partial r u_r \psi}{\partial r} + \frac{1}{r}\frac{\partial v_\phi \psi}{\partial \phi} + \frac{\partial w \psi}{\partial z} = 0. \tag{6}$$

Next, we apply the volume average $\frac{1}{\pi \mathbb{R}^2 D}\int_{z=0}^{z=D}\int_{r=0}^{r=\mathbb{R}}\int_{\phi=0}^{\phi=2\pi} r\,d\phi\,dr\,dz$, where $\mathbb{R}$ is the radius at which $V_{PG,IN}$ becomes negligibly small relative to $V_{0,IN}$ and D is the depth of the conditionally unstable layer. Both $\mathbb{R}$ and D define a "control volume," which is wider than the updraft itself. These operations result in the following equation:

$$\frac{d\langle\psi\rangle}{dt} + 2\frac{\widehat{u_r\psi}|_{r=\mathbb{R}}}{\mathbb{R}} + \frac{\overline{w\psi}|_{z=H}}{D} = 0, \tag{7}$$

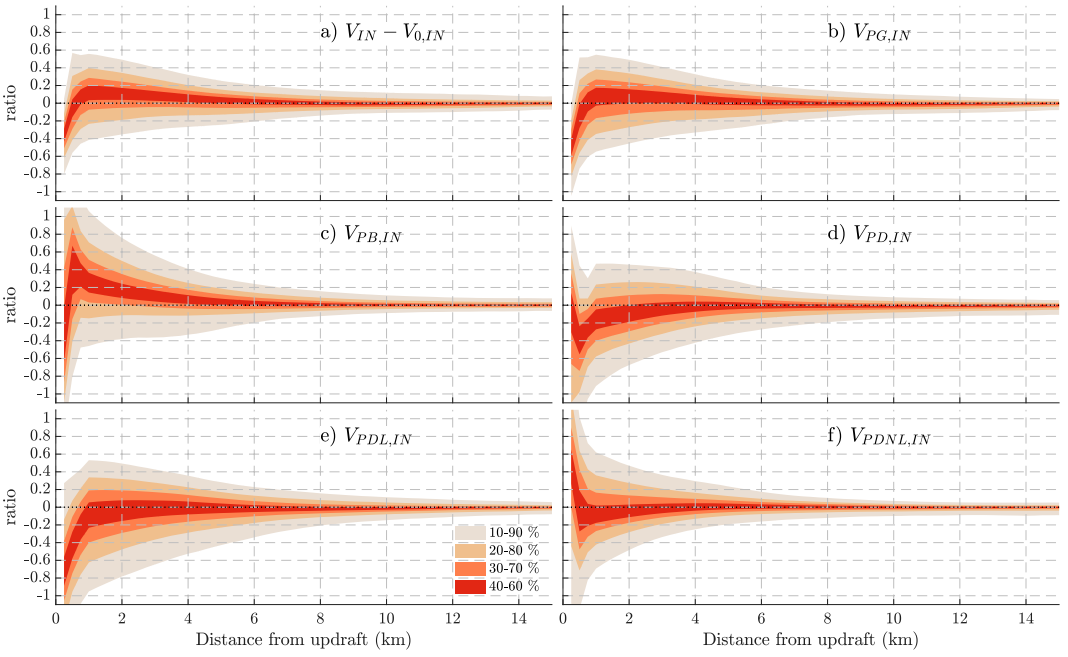

FIG. 10. Parcel distance from the updraft edge (km, x axis) vs the ratios (unitless, y axis) of different inflow components to the background cloud-relative flow, for parcels in all of the s1 and s2 simulations. The darkest shaded region represents the 40th–60th-percentile range among trajectories, and progressively lighter shading represents progressively larger percentile ranges (at intervals of 10%), with the lightest color showing the 10th–90th percentiles. This analysis only considers trajectories that enter updrafts prior to updraft maximum w exceeding 40 m s^{-1}, which we define as the nascent stage of cloud growth. The updraft edge is defined as the first instance of a parcel's w exceeding 3 m s^{-1}, for a parcel whose maximum w eventually exceeds 10 m s^{-1}.

where $\widehat{u_r\psi}|_{r=\mathbb{R}}$ is the surface-area-averaged lateral flux of ψ through the side of the control volume, $\overline{w\psi}|_{z=H}$ is the area averaged vertical flux of ψ through the top of the control volume, and $d\langle\psi\rangle/dt$ represents the time tendency of conditional instability in the control volume due to convection. Because we have chosen $\mathbb{R}$ to be sufficiently far from the updraft so that $\mathbf{V}_{\rm PG}$ vanishes, we may replace u_r with $V_{\rm CR}/\pi$, which is the average radial component of $\mathbf{V}_{\rm CR}$ at a given height. Finally, we write the flux terms as a sum of negative (outward, denoted by subscript "out") and positive (inward, denoted by subscript "in") fluxes, such that

$$\frac{d\langle\psi\rangle}{dt} + \frac{2}{\pi\mathbb{R}}\left(\widehat{V_{CR}\psi}\big|_{\rm out} - \widehat{V_{\rm CR}\psi}\big|_{\rm in}\right) + \frac{\overline{w\psi}\big|_{\rm out} - \overline{w\psi}\big|_{\rm in}}{D} = 0. \quad (8)$$

A schematic shown in Fig. 12 facilitates the physical interpretation of these individual terms. For instance, $\widehat{V_{\rm CR}\psi}|_{\rm in}$ represents the influx of conditional instability into the control volume on the volume's upstream side. $\widehat{V_{\rm CR}\psi}|_{\rm out}$ represents the outward flux of convectively modified air on the downstream side of the control volume, which contains a mix of downdraft and conditionally unstable air. $\overline{w\psi}|_{\rm out}$ represents the vertical flux of conditional instability out of the volume via an updraft, and $\overline{w\psi}|_{\rm in}$ represents the downward flux of convectively stable air into the volume via downdrafts.

Since inflowing convectively unmodified air ought to be conditionally unstable, we set $\psi = 1$ for these parcels and hence $\widehat{V_{\rm CR}\psi}|_{\rm in} = \widehat{V_{\rm CR}}$. A reasonable assumption for laterally outflowing air is that its mixture of convectively unstable and stable air is equal to that of the control volume, and hence we set $\psi = \langle\psi\rangle$ here. We further make the approximation that $\widehat{V_{\rm CR}\psi}|_{\rm out} \approx \widehat{V_{\rm CR}}\langle\psi\rangle$. Since vertically outflowing air in updrafts is likely convectively unstable, we set $\psi = 1$ here and hence $\overline{w\psi}|_{\rm out} = \overline{w}|_{\rm out}$. Finally, since air within downdrafts should not be convectively unstable, we assume that $\psi = 0$ here, and hence $\overline{w\psi}|_{\rm in} = 0$.

We may rewrite $\overline{w}|_{\rm out}$ in terms of the updraft radius R and the average updraft velocity $w_{\rm ud}$ as $\overline{w}|_{\rm out} = w_{\rm ud}R^2/\mathbb{R}^2$. Finally, we note from our analysis of Fig. 10 that $\mathbb{R} \approx 2R$ is a reasonable approximation, implying that $|\mathbf{V}_{\rm PG}|$ becomes negligible at a distance of R from the updraft edge. Applying all of these assumptions and substitutions gives

$$\frac{d\langle\psi\rangle}{dt} - \frac{V_{\rm CR}}{\pi R}(1 - \langle\psi\rangle) + \frac{w_{\rm ud}}{4D} = 0. \quad (9)$$

With the initial condition of $\langle\psi\rangle(0) = 1$, we obtain the following analytic solution to Eq. (9):

$$\langle\psi\rangle(t) = \frac{\pi w_{\rm ud}R}{4DV_{\rm CR}}\left\{e^{-[V_{\rm CR}/(\pi R)]t} - 1\right\} + 1. \quad (10)$$

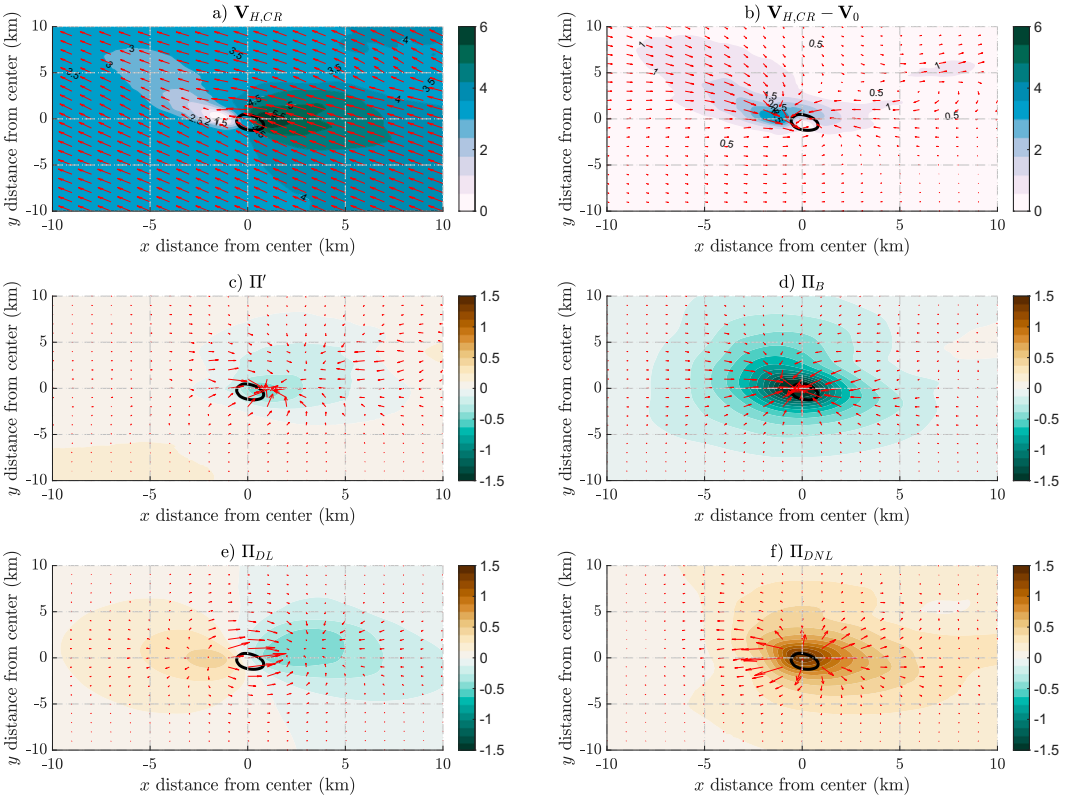

FIG. 11. Plan views at 1.05 km AGL of the updraft-centered composites of all CAPE2 simulations during the nascent cloud stage, defined as the time period where the maximum w was between 10 and 40 m s^{-1}. The 3 m s^{-1} w contour is shown in black in all panels. (a) $\mathbf{V}_{H,\mathrm{CR}}$ relative magnitudes (red arrows) and speed (m s^{-1}, color shading). (b) As in (a), but showing $\mathbf{V}_{H,\mathrm{CR}} - \mathbf{V}_0$. (c)–(f) Individual Π components (1×10^{-4}, nondimensional, color shading) at 1.05 km AGL, and the direction and relative magnitude of the associated horizontal acceleration (red arrows). (c) Total Π', (d) Π_B, (e) Π_{DL}, (f) Π_{DNL}.

Finally, we solve for the time scale τ of total instability dissipation from the volume by setting $\langle\psi\rangle(\tau) = 0$:

$$\tau = -\frac{\pi R}{V_{\mathrm{CR}}}\ln\left(1 - \frac{4DV_{\mathrm{CR}}}{\pi w_{\mathrm{ud}}R}\right). \tag{11}$$

In the special case of $V_{\mathrm{CR}} = 0$, the right-hand side of Eq. (11) is undefined. However, τ in this case is obtained by simply integrating Eq. (9) as

$$\tau = \frac{4D}{w_{\mathrm{ud}}}. \tag{12}$$

For an updraft with radius R that exists within a conditionally unstable layer of depth D, and that has an updraft speed w_{ud} at the top of the conditionally unstable layer, τ tells how long the updraft will entirely replace its local supply of conditionally unstable air with outflow.

Figure 13 displays the behavior of τ as a function of R and V_{CR}, with $D = 2$ km, which is roughly consistent with the depth of the conditionally unstable layer in the WK82 sounding (Nowotarski et al. 2020), and for $w_{\mathrm{ud}} = 5$ m s^{-1} (Fig. 13a), 7.5 m s^{-1} (Fig. 13b), 10 m s^{-1} (Fig. 13c), and 12.5 m s^{-1} (Fig. 13d). These w_{ud} values are consistent with horizontally averaged updraft w at 2 km AGL (not shown) in the simulations, which ranged from 5 to 15 m s^{-1}. Notably, there is a threshold in V_{CR}, above which τ is imaginary implying that instability will never be depleted and an updraft may be sustained indefinitely, and below which τ is real indicating that instability will be depleted over a finite time scale and an updraft will decay. Furthermore, as R increases, the threshold of V_{CR} required for an indefinitely sustained updraft also increases. This dependency reflects that wider updrafts more quickly consume instability, and must have a faster resupply of conditionally unstable air via V_{CR}. In the region of the parameter space where τ is real, typical magnitudes of τ are on the order of 10–30 min for $w_{\mathrm{ud}} \geq 7.5$ m s^{-1} (Figs. 13b–d), and 20–60 min for $w_{\mathrm{ud}} < 7.5$ m s^{-1} (Fig. 13a). Thus, in general, a critical threshold of V_{CR} is necessary to sustain an updraft and prevent the updraft from running out of conditionally unstable "fuel." If this critical threshold of V_{CR} is not met, an updraft will exhaust conditionally unstable air faster than it is resupplied, and the updraft will decay over a time scale of minutes. Note that the conclusions from this analysis are consistent with those of Peters et al. (2019b), in that the updraft R ought to positively depend on V_{CR}. Yet we have completely avoided the need to assume that $|V_{\mathrm{IN}}| \approx |V_{\mathrm{CR}}|$, or to assume anything

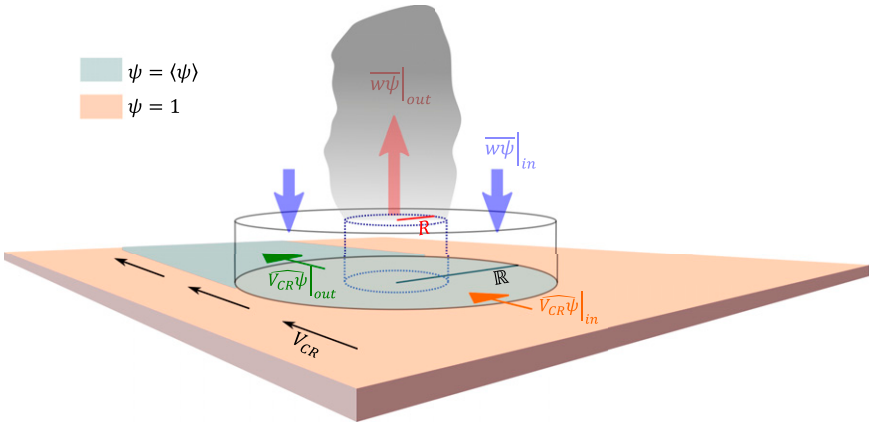

FIG. 12. Schematic that visually depicts the individual terms in Eq. (8), and their connection to physical processes within and near a cloud. The "control volume" is the outer cylinder with radius $\mathbb{R}$, and the cross-sectional area of the updraft is represented by the inner cylinder with radius R. The gray shaded region and upward red arrow represents the cloudy updraft, which corresponds to $\overline{w\psi}|_{\text{out}}$. The downward blue arrows represent downdrafts, and correspond to $\overline{w\psi}|_{\text{in}}$. The orange and green arrows correspond to $\widehat{V_{\text{CR}}\psi}|_{\text{in}}$ and $\widehat{V_{\text{CR}}\psi}|_{\text{out}}$, respectively. Orange shaded regions represent convectively unstable flow with $\psi = 1$, and green shaded regions represent convectively modified air with $\psi = \langle\psi\rangle$ that is exiting the control volume.

about the pressure features of the updraft. All that we have assumed is that the distance $\mathbb{R}$ over which $|\mathbf{V}_{\text{PG}}|$ is nonnegligible is equal to $2R$, which is completely consistent with the behavior of the simulations. In fact, the basic tenet of the idea is retained if we select $\mathbb{R} = nR$, where n is a positive number (not shown), albeit the exact values of τ and the position in the V_{CR} versus R parameter space where τ flips from real to imaginary change somewhat.

To understand a bit more about the physical processes within the updraft that accelerate inward flowing parcels, we further partition $\mathbf{V}_{\text{PG}}$ into $\mathbf{V}_B$, $\mathbf{V}_{\text{DL}}$, and $\mathbf{V}_{\text{DNL}}$ that result from three different respective pressure components Π'_B, Π'_{DL}, and Π'_{DNL}. These pressure components are defined by solving the following Poisson equations:

$$\nabla \cdot (c_{\text{pd}}\rho_0\theta_{\rho,0}\nabla\Pi_B) = \frac{\partial \rho_0 B}{\partial z}, \tag{13}$$

$$\nabla \cdot (c_{\text{pd}}\rho_0\theta_{\rho,0}\nabla\Pi_{\text{DL}}) = \rho_0 \nabla w \cdot \frac{\partial \mathbf{V}_0}{\partial z}, \tag{14}$$

$$\nabla \cdot (c_{\text{pd}}\rho_0\theta_{\rho,0}\nabla\Pi_{\text{DNL}}) = \nabla \cdot \rho_0[(\mathbf{V}' \cdot \nabla)\mathbf{V}'], \tag{15}$$

where $\mathbf{V}$ is the three-dimensional wind vector, and $\mathbf{V}' = \mathbf{V} - \mathbf{V}_0$ is a perturbation from the initial reference wind profile. The partitioning of the Π terms into these three components facilitates the attribution of different physical processes to parcel accelerations. The Π_{DL} term is colloquially known as "linear dynamic pressure," and the Π_{DNL} term is colloquially known as "nonlinear dynamic pressure" (e.g., Markowski and Richardson 2010). Both of these pressure terms relate to spatial gradients in flow velocity, and both are thought to increase their magnitude as shear increases. For instance, Π_{DL} is influenced by an updraft's interaction with vertically sheared flow. The Π_{DNL} term is influenced by strong rotation or deformation within the updraft, such as in the vicinity of a mesocyclone or the toroidal circulations of thermals. The Π_B term is colloquially known as "buoyancy pressure," and relates to the thermodynamic response of the atmosphere to a region of nonzero buoyancy, and is ubiquitous among all buoyant convection. These pressure components are computed by the CM1 source code, and we used trilinear interpolation to interpolate horizontal and vertical accelerations related to these quantities onto trajectory locations every 30 s. These pressure contributions yield the following contributions to $V_{\text{PG,IN}}$: $V_{\text{PDL,IN}}$ which is associated with Π_{DL}, $V_{\text{PDNL,IN}}$, which is associated with Π_{DNL}, $V_{\text{PD,IN}} \equiv V_{\text{PDL,IN}} + V_{\text{PDNL,IN}}$, which is the total contribution by dynamic pressure to the horizontal perturbation wind, and $V_{\text{PB,IN}}$, which is associated with Π_B.

To provide context for the distribution of these pressure fields in our simulations, it is useful to make comparisons to the typical pressure distributions in unsheared convection. For instance, Morrison and Peters (2018) show that Π_B is typically negative at updraft base (see their Fig. 5), with a nearly commensurate positive Π_{DNL} (see their Fig. 6) associated with the horizontal flow convergence induced by the negative Π_B. The sum of these pressure contributions typically results in net negative Π' at updraft base, albeit of a lesser magnitude than would result from Π_B alone (Morrison 2016b). A very similar pattern of negative Π_B inducing inward accelerations (Fig. 11d), and positive Π_{DNL} (Fig. 11f) partially opposing these inward accelerations, was present in the simulations studied here. The primary difference between the sheared updrafts studied here with past studies of unsheared updrafts is the presence of a dipole of Π_{DL} straddling the updraft, with negative Π_{DL} downshear (to the right in Fig. 11e), and positive Π_{DL} upshear (to the left in Fig. 11e). This pattern of Π_{DL} displaced the negative Π' slightly downstream of the updraft

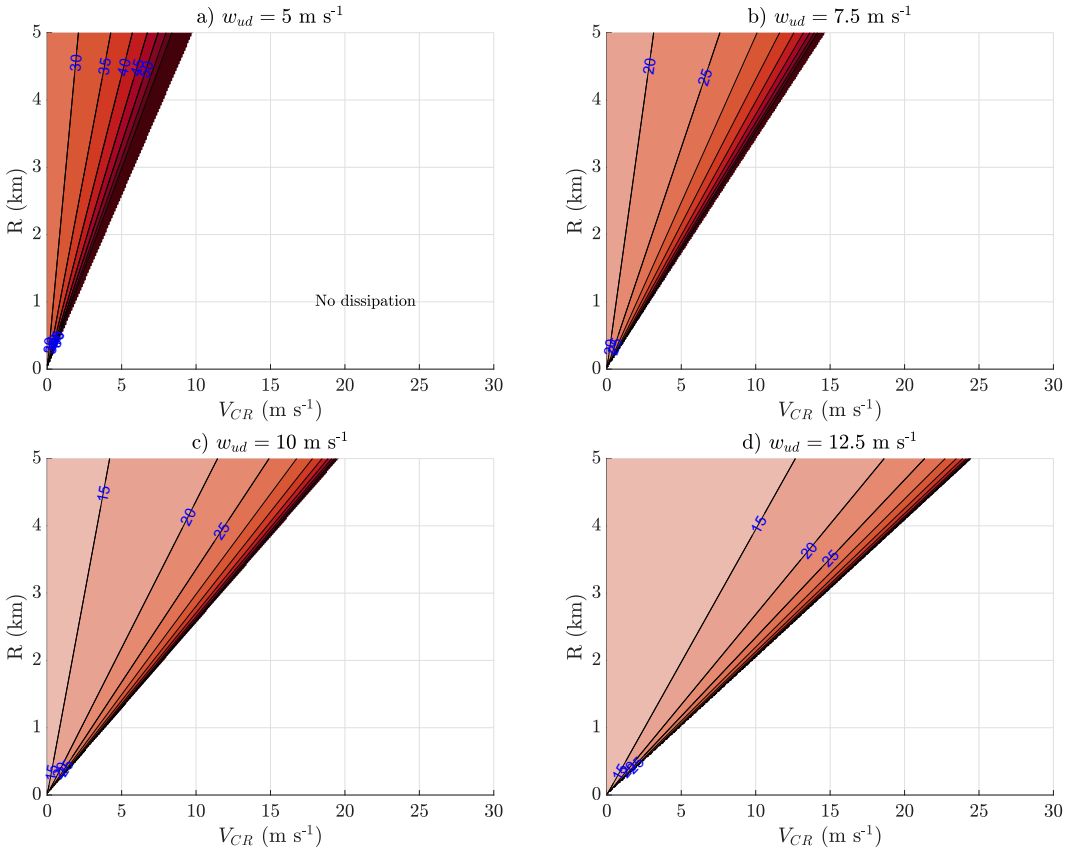

FIG. 13. Theoretical solutions for τ (min, color shading, also see blue contour labels) as a function of V_{CR} (m s^{-1}, x axis) and R (km, y axis). Unshaded regions correspond to imaginary τ (i.e., no updraft dissipation). (a) w_{ud} = 5 m s^{-1}, (b) w_{ud} = 7.5 m s^{-1}, (c) w_{ud} = 10 m s^{-1}, (d) w_{ud} = 12.5 m s^{-1}.

(to the right in Fig. 11c), explaining the patterns of parcel accelerations discussed earlier. In accordance with these Π distributions, local storm-induced inflow was primarily driven by Π_B (Fig. 10c), and to a lesser extent Π_{DNL} (Fig. 10f). This may seem at odds with past studies of sheared storms, which have shown the presence of substantial rotationally driven negative Π_{DNL} in the lower part of updrafts, and have implicated this feature in the propagation of updrafts (Rotunno and Klemp 1982, 1985). However, it is probable that substantial rotation had not yet developed at low levels during nascent updraft stages.

5. After a cloud initially develops, how does it persist?

For a cloud to grow wider and deepen through the processes outlined in the progressive rooting hypothesis, air parcels that approach the cloud within low-level flow must be accelerated upward into the updraft. In the theoretical model and in previous theoretical analyses such as Peters et al. (2019b), we assumed that this upward acceleration occurs without characterizing its mechanism. This assumption has prompted questions from colleagues along the lines of "how does the low-level air approaching the cloud know that it needs to go up?" The simulated trajectories analyzed here provide us with the means to answer the aforementioned question.

To connect vertical accelerations to distinct physical processes, we make use of our decomposition of Π' into Π'_B, Π'_{DL}, and Π'_{DNL} from the previous section to write the anelastic vertical momentum equation as

$$\frac{dw}{dt} = \underbrace{\underbrace{\underbrace{B}_{\text{Buoyancy}} - c_{pd}\theta_{\rho,0}\frac{\partial \Pi_B}{\partial z}}_{\text{BPA}} - c_{pd}\theta_{\rho,0}\frac{\partial \Pi_{DL}}{\partial z}}_{\text{LPA}} - c_{pd}\theta_{\rho,0}\frac{\partial \Pi_{DNL}}{\partial z}}_{\text{NLPA}}, \quad (16)$$

EBPA DYN

where $B \equiv g\left[\theta'/\theta_0 + (R_v/R_d - 1)q'_v - q_t + q_v\right]$ is the formula for buoyancy used in CM1, BPA is buoyancy pressure acceleration, LPA is linear dynamic pressure acceleration, NLPA is nonlinear dynamic pressure acceleration, EBPA is effective buoyancy pressure acceleration (Davies-Jones 2003; Peters 2016), and DYN is total dynamic pressure acceleration. In an analogous manner to what was done with horizontal accelerations, Eq. (16) was temporally integrated along trajectories to obtain individual contributions to w from each of the different acceleration terms on the right-hand side of the equation. These w contributions are w_B, w_{BPA}, w_{LPA}, w_{NLPA}, w_{EBPA}, and w_{DYN}, respectively. We then examined the vertical

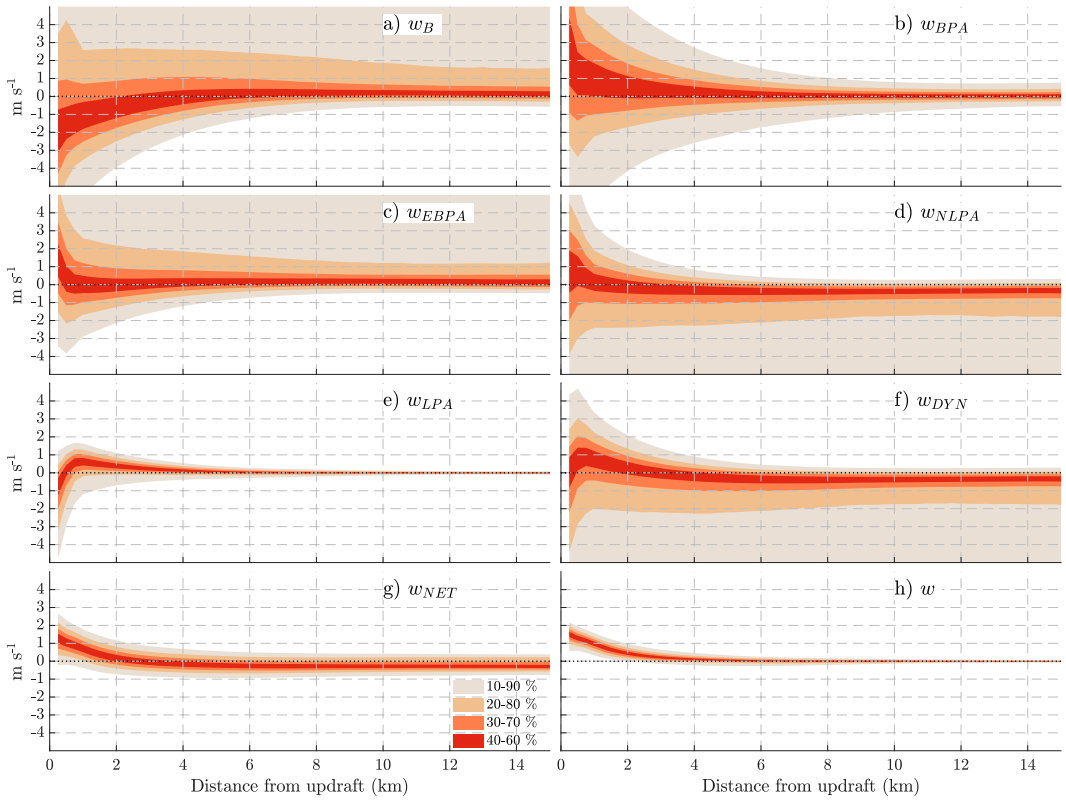

FIG. 14. As in Fig. 10, but showing the contributions by individual accelerations to w (m s^{-1}, y axis) along trajectories as a function of the distance of parcels from the updraft edge (km, x axis), for parcels that entered updrafts during the nascent stages of simulations. Individual terms are (a) w_B, (b) w_{BPA}, (c) w_{EBPA}, (d) w_{NLPA}, (e) w_{LPA}, (f) w_{DYN}, (g) the sum of all terms (w_{NET}), and (h) the actual w along trajectories interpolated from the simulations (w).

profiles of each of these w terms along trajectories during their first 1 km of ascent into updrafts.

Profiles of w_B (Fig. 14a) show a progression from a weak positive contribution distant from the updraft, toward generally negative contributions near the updraft as parcels ascended through their CIN layer and are adiabatically cooled. The corresponding region of weakly negative B is evident in vertical cross sections (Fig. 15a) below updraft base, within regions where parcels make their initial upward turn into the updraft. Despite this negative B and w_B, w is nearly universally positive as parcels approach the updraft (Fig. 14h) due to a preponderance of upward accelerations toward negative Π' near the updraft core (Fig. 15c). w_{BPA} (Fig. 14b) is generally anticorrelated with w_B (Fig. 14a), as theory predicts should be the case (Morrison 2016a). Notably, the sum of these two terms w_{EBPA} (Fig. 14c) is positive in all situations by the time parcels reach the updraft edge, reflecting that despite the presence of some CIN, parcels do not actually experience a net downward thermodynamic acceleration as they ascend into the updraft. This echoes an important finding in Brown and Nowotarski (2019), wherein their Fig. 14b also shows vanishing EBPA for parcels entering simulated updrafts. The net positive EBPA near updraft base (Fig. 15b) occurs because of the presence of positive B within the updraft (Fig. 15a) and the associated negative Π_B at the updraft base (Fig. 15d).

Contributions from w_{LPA} (Fig. 14e) were generally positive and of comparable magnitude to w_{EBPA} (Fig. 14c). This positive w_{LPA} was driven by relatively weak, albeit spatially expansive, upward accelerations below the negative Π_{DL} along the eastern updraft flank (Fig. 15e). The largest contribution to w as parcels approached their LFCs occurred from w_{NLPA} (Fig. 14d), which contributed to a net positive w_{DYN} (Fig. 14f) of comparable magnitude to w_{EBPA} (Fig. 14c). This positive w_{DYN} occurred because of the presence of a strong negative Π_{DNL} region within the updraft core and just above the height of maximum w (Fig. 15f). This strong negative Π_{DNL} was likely related to vorticity associated with the downstream baroclinically generated toroidal circulation of the updraft (Fig. 15a), and/or vertical vorticity maxima associated with the tilting of ambient horizontal vorticity by the updraft (Fig. 15f). Thus, persistent upward accelerations from Π_{DNL} were primarily responsible for lifting new inflowing parcels to their LFCs and cloud maintenance. This finding is consistent with that of Marion and Trapp (2019), who argued that vertical accelerations at low levels associated with Π_{DL} and Π_{DNL} were responsible for widening and perpetuating nascent supercell updrafts.

A natural question at this point is, why then do updrafts sometimes decay with time if such pressure features are persistently present? The magnitude of pressure perturbations

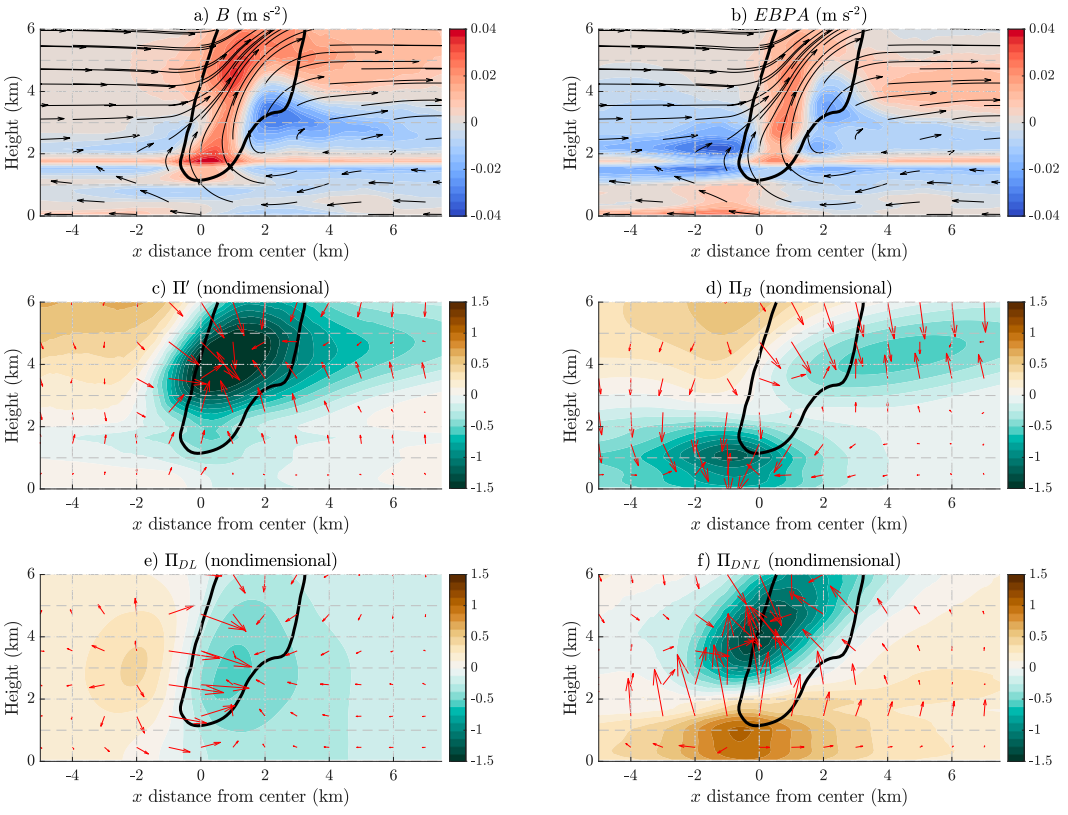

FIG. 15. Vertical cross sections from the nascent stages of updrafts, showing updraft-centered composites of (a) B (m s^{-2}, color shading) and cloud-relative streamlines (black arrows), (b) EBPA (m s^{-2}, color shading), (c) Π' (1×10^{-4}, nondimensional, color shading), (d) Π_B (1×10^{-4}, nondimensional, color shading), (e) Π_{DL} (1×10^{-4}, nondimensional, color shading), and (f) Π_{DNL} (1×10^{-4}, nondimensional, color shading). The 3 m s^{-1} w contour is shown in black. Arrows in (c)–(f) show the relative magnitude and direction of accelerations associated with the Π component shaded in the panel.

are generally correlated with updraft attributes. For example, the magnitude of Π_{DL} and Π_{DNL} relates to w (among other things). Furthermore, these Π features also depend on spatial gradients in the horizontal wind. For instance, both of these pressure features act to "deflect upward" the incoming V_{CR}, as was discussed in the previous subsection. If V_{CR} decreases over time, so will the magnitude of the horizontal gradients in wind near updraft base and consequently the magnitude of Π. Thus, changes to the updraft in time will feed back to the region of low-level accelerations below the updraft. In the scenario described by our hypothesis wherein updrafts do not undergo progressive rooting and eventually decay, entrainment-driven dilution will lead to reductions in updraft w and V_{CR} over time. As w and V_{CR} decrease, so will the magnitudes of Π_{DL} and Π_{DNL}, and thus w_{DYN}. Further, as B decreases, so will the magnitude of Π_B. Thus, the behavior of the region of subcloud lifting that supplies the updraft is intrinsically connected to the behavior of the updraft in the free troposphere.

6. Summary, discussion, and conclusions

This article addresses a hypothesis that was developed in Part I for how vertical wind shear influences deep convection initiation (DCI). This hypothesis is directly quoted from Part I as, "nascent convective updrafts of sufficient width increase their updraft-relative inflow upon encountering environmental wind shear. Updrafts widen because of this increased inflow, which reduces their susceptibility to entrainment-driven dilution. From this process, clouds can progressively 'root' into a deeper steering current, furthering this positive feedback cycle. Updrafts eventually achieve a steady width, w, depth, and motion. Under situations for which progressive rooting occurs, the deleterious effects of shear-induced downward pressure gradient accelerations are counteracted."

To evaluate the hypothesis from Part I, we compared the behavior of the theoretical model to numerical simulations of convection that were run over a range of convective environments. Our conclusions are as follows:

- Both the simulations and the theoretical model show a pronounced bifurcation in outcomes, whereby updrafts with initial radii R_0 above a threshold developed into quasi-steady deep convective updrafts, and updrafts with R_0 below said threshold decay over a time scale of an hour or less.
- In the theoretical model, updraft growth (or the lack thereof) was regulated by changes to cloud motion, cloud-

relative flow V_{CR}, and updraft depth. An evaluation of these variables in the simulations shows very similar behavior to that of the theoretical model.
- DCI characteristics in the simulations display similar environmental dependencies on shear s, free-tropospheric relative humidity RH, and convective available potential energy (CAPE) to those of the theoretical model.
- A detailed analysis of horizontal accelerations within cloud inflow supports the idea that inflow is strongly regulated by V_{CR}, which was a key assumption in the theoretical model.
- A detailed analysis of vertical accelerations within cloud inflow shows that vertical accelerations from dynamic pressure perturbations are the primary mechanism that lifts subcloud inflow to its LFC, which is consistent with the arguments in Marion and Trapp (2019).

Our conclusions provide some reconciliation between previous work, which has focused on the analysis of accelerations related to dynamic pressure perturbations to explain the role of vertical wind shear in determining the temporal evolution of updraft width (Marion and Trapp 2019), and our work, which has focused on the interplay between cloud depth, cloud motion, cloud-relative flow, and entrainment in how updraft width evolves with time. Our theoretical approach in Part I does not neglect low-level pressure accelerations. Rather, we assume that such pressure accelerations exist, but we do not treat them explicitly in order to make our system of equations solvable. Thus, we do not believe that these approaches are mutually exclusive. Rather, the two ideas must go hand-in-hand. For instance, a wide region low-level dynamic lifting cannot sustain a wide updraft if there is not sufficient cloud-relative flow to resupply conditional instability that is exhausted by the updraft. We may also invert this argument: a wide updraft cannot exist within large cloud-relative flow unless there is a sufficiently large region of dynamic and/or buoyancy pressure accelerations to accelerate the flow upward into an updraft.

It *may* be possible for an updraft to be persistently narrow while experiencing large low-level cloud-relative flow because the updraft has a narrow low-level dynamic and/or buoyant pressure "footprint." However, such a situation seems unlikely to persist indefinitely. If viewed from the perspective of our progressive rooting hypothesis, then the updraft will either dissipate due to entrainment because it is narrow, or progressively widen because it roots within a deeper steering current and increases its inflow. If the situation is viewed through the hypothesis of Marion and Trapp (2019), then the updraft's dynamic pressure "footprint" is likely to cause the updraft to widen with time. Again, both of these explanations offer two different perspectives on the same process. We do, however, feel that there are certain unique advantages of our theoretical approach, which provides detailed explanations for why widening happens in some situations and not others, how wide and deep updrafts will get, and why they will eventually stop widening and deepening with time (see Part I).

We have not explicitly considered cold pools and their potential role in DCI. During the nascent stages of the updrafts in our simulations, cold pools were not well developed, which validates our approach neglecting their influence. However, DCI in the real world often occurs in the presence of preexisting outflow from convection, and DCI in these cases is undoubtedly influenced by those outflow boundaries. The basic tenet of some ideas should be unchanged in the presence of cold pools. For instance, mass continuity will be obeyed regardless of the presence or absence of a cold pool. However, cold pools may result in substantial alterations to cloud motion that are not accounted for in our framework, which assumes clouds are advected by the cloud-bearing wind. We have also neglected the role of externally driven mesoscale lifting on DCI (e.g., terrain, low-level jets). Needless to say, we have only begun to break ground on understanding what is undoubtedly a very complex process in the atmosphere, and numerous future investigations of various yet-to-be-explored avenues are warranted.

Acknowledgments. J. Peters's and J. Mulholland's efforts were supported by National Science Foundation (NSF) Grants AGS-1928666 and AGS-1841674, and the Department of Energy Atmospheric System Research (DOE ASR) Grant DE-SC0000246356. H. Morrison was supported by DOE ASR Grant DE-SC0020104. J. Marquis's and T. Nelson's efforts were supported by NSF Grant AGS-1661707. J. Marquis was also supported by DOE's Science Biological and Environmental Research as part of the ASR program, with work conducted at the Pacific Northwest National Laboratory. C. Nowotarski's efforts were supported by NSF Grant AGS-1928319. The National Center for Atmospheric Research is sponsored by NSF. We thank Kamal Kant Chandrakar for previously modifying CM1 to apply the surface flux based forcing method for deep convection initiation. We also thank three anonymous peer reviewers for their helpful feedback, which greatly improved the manuscript.

Data availability statement. All scripts and namelists used to generate data for this study are available via Figshare at https://figshare.com/articles/dataset/CI_PAPER/14515560.

REFERENCES

Brown, M., and C. J. Nowotarski, 2019: The influence of lifting condensation level on low-level outflow and rotation in simulated supercell thunderstorms. *J. Atmos. Sci.*, **76**, 1349–1372, https://doi.org/10.1175/JAS-D-18-0216.1.

Bryan, G. H., and J. M. Fritsch, 2002: A benchmark simulation for moist nonhydrostatic numerical models. *Mon. Wea. Rev.*, **130**, 2917–2928, https://doi.org/10.1175/1520-0493(2002)130<2917:ABSFMN>2.0.CO;2.

Chavas, D. R., and D. T. Dawson, 2021: An idealized physical model for the severe convective storm environmental sounding. *J. Atmos. Sci.*, **78**, 653–670, https://doi.org/10.1175/JAS-D-20-0120.1.

Davies-Jones, R., 2003: An expression for effective buoyancy in surroundings with horizontal density gradients. *J. Atmos. Sci.*, **60**, 2922–2925, https://doi.org/10.1175/1520-0469(2003)060<2922:AEFEBI>2.0.CO;2.

Klemp, J. B., and R. B. Wilhelmson, 1978: Simulations of right- and left-moving storms produced through storm splitting. *J. Atmos. Sci.*, **35**, 1097–1110, https://doi.org/10.1175/1520-0469(1978)035<1097:SORALM>2.0.CO;2.

Lebo, Z. J., and H. Morrison, 2015: Effects of horizontal and vertical grid spacing on mixing in simulated squall lines and implications for convective strength and structure. *Mon. Wea. Rev.*, **143**, 4355–4375, https://doi.org/10.1175/MWR-D-15-0154.1.

Lin, Y., and K. E. Mitchell, 2005: The NCEP stage II/IV hourly precipitation analyses. *19th Conf. on Hydrology*, San Diego, CA, Amer. Meteor. Soc., 1.2, https://ams.confex.com/ams/pdfpapers/83847.pdf.

Marion, G. R., and R. J. Trapp, 2019: The dynamical coupling of convective updrafts, downdrafts, and cold pools in simulated supercell thunderstorms. *J. Geophys. Res. Atmos.*, **124**, 664–683, https://doi.org/10.1029/2018JD029055.

Markowski, P., and Y. Richardson, 2010: *Mesoscale Meteorology in Midlatitudes*. Wiley-Blackwell, 430 pp.

Mitchell, K. E., and Coauthors, 2004: The multi-institution North American Land Data Assimilation System (NLDAS): Utilizing multiple GCIP products and partners in a continental distributed hydrological modeling system. *J. Geophys. Res.*, **109**, D07S90, https://doi.org/10.1029/2003JD003823.

Morrison, H., 2016a: Impacts of updraft size and dimensionality on the perturbation pressure and vertical velocity in cumulus convection. Part I: Simple, generalized analytic solutions. *J. Atmos. Sci.*, **73**, 1441–1454, https://doi.org/10.1175/JAS-D-15-0040.1.

——, 2016b: Impacts of updraft size and dimensionality on the perturbation pressure and vertical velocity in cumulus convection. Part II: Comparison of theoretical and numerical solutions and fully dynamical simulations. *J. Atmos. Sci.*, **73**, 1455–1480, https://doi.org/10.1175/JAS-D-15-0041.1.

——, and J. M. Peters, 2018: Theoretical expressions for the ascent rate of moist convective thermals. *J. Atmos. Sci.*, **75**, 1699–1719, https://doi.org/10.1175/JAS-D-17-0295.1.

——, G. Thompson, and V. Tatarskii, 2009: Impact of cloud microphysics on the development of trailing stratiform precipitation in a simulated squall line: Comparison of one- and two-moment schemes. *Mon. Wea. Rev.*, **137**, 991–1007, https://doi.org/10.1175/2008MWR2556.1.

——, J. M. Peters, K. K. Chandakar, and S. C. Sherwood, 2021: Influences of environmental relative humidity and horizontal scale of subcloud ascent on deep convective initiation. *J. Atmos. Sci.*, **79**, 337–359, https://doi.org/10.1175/JAS-D-21-0056.1.

Moser, D. H., and S. Lasher-Trapp, 2017: The influence of successive thermals on entrainment and dilution in a simulated cumulus congestus. *J. Atmos. Sci.*, **74**, 375–392, https://doi.org/10.1175/JAS-D-16-0144.1.

Nelson, T. C., J. N. Marquis, J. M. Peters, and K. Friedrich, 2021: Cloud-scale simulations of convection initiation using observed near-cloud environments from RELAMPAGO-CACTI. *2020 Fall Meeting*, Online, Amer. Geophys. Union, Abstract A085-0007, https://agu.confex.com/agu/fm20/meetingapp.cgi/Paper/683839.

Nowotarski, C. J., J. M. Peters, and J. P. Mulholland, 2020: Evaluating the effective inflow layer of simulated supercell updrafts. *J. Atmos. Sci.*, **148**, 3507–3532, https://doi.org/10.1175/MWR-D-20-0013.1.

Parker, M. D., 2014: Composite VORTEX2 supercell environments from near-storm soundings. *Mon. Wea. Rev.*, **142**, 508–529, https://doi.org/10.1175/MWR-D-13-00167.1.

Peters, J. M., 2016: The impact of effective buoyancy and dynamic pressure forcing on vertical velocities within two-dimensional updrafts. *J. Atmos. Sci.*, **73**, 4531–4551, https://doi.org/10.1175/JAS-D-16-0016.1.

——, and D. R. Chavas, 2021: Evaluating the conservation of energy variables in simulations of deep moist convection. *J. Atmos. Sci.*, **78**, 3229–3246, https://doi.org/10.1175/JAS-D-20-0351.1.

——, W. M. Hannah, and H. Morrison, 2019a: The influence of vertical wind shear on moist thermals. *J. Atmos. Sci.*, **76**, 1645–1659, https://doi.org/10.1175/JAS-D-18-0296.1.

——, C. Nowotarski, and H. Morrison, 2019b: The role of vertical wind shear in modulating maximum supercell updraft velocities. *J. Atmos. Sci.*, **76**, 3169–3189, https://doi.org/10.1175/JAS-D-19-0096.1.

——, H. Morrison, C. J. Nowotarski, J. P. Mulholland, and R. L. Thompson, 2020a: A formula for the maximum vertical velocity in supercell updrafts. *J. Atmos. Sci.*, **77**, 3747–3757, https://doi.org/10.1175/JAS-D-20-0103.1.

——, C. J. Nowotarski, and J. P. Mulholland, 2020b: The influences of effective inflow layer streamwise vorticity and storm-relative flow on supercell updraft properties. *J. Atmos. Sci.*, **77**, 3033–3057, https://doi.org/10.1175/JAS-D-19-0355.1.

——, D. R. Chavas, and J. P. Mulholland, 2021: Generalized lapse rate formulas for use in entraining CAPE calculations. *J. Atmos. Sci.*, **79**, 815–836, https://doi.org/10.1175/JAS-D-21-0118.1.

——, H. Morrison, T. C. Nelson, J. N. Marquis, J. P. Mulholland, and C. J. Nowotarski, 2022: The influence of shear on deep convection initiation: Part I: Theory. *J. Atmos. Sci.*, **79**, 1669–1690, https://doi.org/10.1175/JAS-D-21-0145.1.

Rotunno, R., and J. B. Klemp, 1982: The influence of the shear-induced pressure gradient on thunderstorm motion. *Mon. Wea. Rev.*, **110**, 136–151, https://doi.org/10.1175/1520-0493(1982)110<0136:TIOTSI>2.0.CO;2.

——, and ——, 1985: On the rotation and propagation of simulated supercell thunderstorms. *J. Atmos. Sci.*, **42**, 271–292, https://doi.org/10.1175/1520-0469(1985)042<0271:OTRAPO>2.0.CO;2.

Schiro, K. A., F. Ahmed, S. E. Giangrande, and J. D. Neelin, 2018: GoAmazon2014/5 campaign points to deep-inflow approach to deep convection across scales. *Proc. Nat. Acad. Sci. USA*, **115**, 4577–4582, https://doi.org/10.1073/pnas.1719842115.

Shima, S.-I., and W. W. Grabowski, 2020: Isolated cumulus congestus based on SCMS campaign: Comparison between Eulerian bin and Lagrangian particle-based microphysics. *Int. Cloud Modeling Workshop 2020*, Online, ICCP, https://iccp2020.tropmet.res.in/assets/ICMW2020_cumulus_congestus.pdf.

Trapp, R., and J. M. Woznicki, 2017: Convective induced stabilizations and subsequent recovery with supercell thunderstorms during the Mesoscale Predictability Experiment (MPEX). *Mon. Wea. Rev.*, **145**, 1739–1754, https://doi.org/10.1175/MWR-D-16-0266.1.

Warren, R. A., H. Richter, H. A. Ramsay, S. T. Siems, and M. J. Manton, 2017: Impact of variations in upper-level shear on simulated supercells. *Mon. Wea. Rev.*, **145**, 2659–2681, https://doi.org/10.1175/MWR-D-16-0412.1.

Weisman, M. L., and J. B. Klemp, 1982: The dependence of numerically simulated convective storms on vertical wind shear and buoyancy. *Mon. Wea. Rev.*, **110**, 504–520, https://doi.org/10.1175/1520-0493(1982)110<0504:TDONSC>2.0.CO;2.

——, and Coauthors, 2015: The Mesoscale Predictability Experiment (MPEX). *Bull. Amer. Meteor. Soc.*, **96**, 2127–2149, https://doi.org/10.1175/BAMS-D-13-00281.1.